

See discussions, stats, and author profiles for this publication at: <https://www.researchgate.net/publication/264044118>

# A Guide to the Implementation of Boundary Conditions in Compact High-Order Methods for Compressible Aerodynamics

**Conference Paper** · June 2014

DOI: 10.2514/6.2014-2923

CITATIONS

8

READS

588

**7 authors**, including:



**Gianmarco Mengaldo**

California Institute of Technology

**19** PUBLICATIONS **257** CITATIONS

[SEE PROFILE](#)



**Daniele De Grazia**

Rolls-Royce

**7** PUBLICATIONS **204** CITATIONS

[SEE PROFILE](#)



**Joaquim Peiro**

Imperial College London

**146** PUBLICATIONS **3,617** CITATIONS

[SEE PROFILE](#)



**Freddie David Witherden**

Imperial College London

**16** PUBLICATIONS **156** CITATIONS

[SEE PROFILE](#)

**Some of the authors of this publication are also working on these related projects:**



Numerical simulations of wind turbine wakes [View project](#)



Design optimisation of tunnel ventilation systems [View project](#)

# A Guide to the Implementation of Boundary Conditions in Compact High-Order Methods for Compressible Aerodynamics

Mengaldo G.\* De Grazia D.<sup>†</sup> Peiro J. <sup>‡</sup>

Farrington A. <sup>§</sup> Witherden F. <sup>¶</sup> Vincent P. E. <sup>¶</sup> Sherwin S.J. <sup>||</sup>

*Imperial College London, South Kensington Campus, London SW7 2AZ, UK*

The nature of boundary conditions, and how they are implemented, can have a significant impact on the stability and accuracy of a Computational Fluid Dynamics (CFD) solver. The objective of this paper is to assess how different boundary conditions impact the performance of compact discontinuous high-order spectral element methods (such as the discontinuous Galerkin method and the Flux Reconstruction approach), when these schemes are used to solve the Euler and compressible Navier-Stokes equations on unstructured grids. Specifically, the paper will investigate inflow/outflow and wall boundary conditions. In all studies the boundary conditions were enforced by modifying the boundary flux. For Riemann invariant (characteristic), slip and no-slip conditions we have considered a direct and an indirect enforcement of the boundary conditions, the first obtained by calculating the flux using the known solution at the given boundary while the second achieved by using a ghost state and by solving a Riemann problem. All computations were performed using the open-source software Nektar++ ([www.nektar.info](http://www.nektar.info)).

## Nomenclature

$\hat{\mathbf{n}}$	Normal vector
$x, y, z$	Cartesian coordinates
$V_n$	Normal velocity $m/s$
$\mathbf{V}$	Velocity vector $m/s$
$u, v, w$	x-, y- and z-components of the velocity $m/s$
$\mathbf{q}$	Vector of conserved variables of the compressible Euler or Navier-Stokes equations
$\mathbf{f}_i, \mathbf{f}_i, \mathbf{h}_i$	Inviscid flux components of the compressible Euler or Navier-Stokes equations
$\mathbf{f}_v, \mathbf{g}_v, \mathbf{h}_v$	Viscous flux components of the compressible Navier-Stokes equations
$\mathbf{f}, \mathbf{g}, \mathbf{h}$	Total flux components of the compressible Navier-Stokes equations
$\rho$	Density $kg/m^3$
$E$	Total energy $Pa$
$\gamma$	Ratio of the specific heats
$k$	Thermal conductivity $W/mK$
$p$	Pressure $Pa$
$T$	Temperature $K$
$\mathbf{M}, \mathbf{S}, \mathbf{b}$	Mass matrix, advection matrix and boundary term
$\tilde{\mathcal{H}}$	Tensor of the fluxes

---

\*PhD student, Department of Aeronautics and Mathematics, Imperial College London, London SW7 2AZ, UK. AIAA member. Corresponding author, email: [g.mengaldo11@imperial.ac.uk](mailto:g.mengaldo11@imperial.ac.uk)

<sup>†</sup>PhD student, Department of Aeronautics and Mathematics, Imperial College London, London SW7 2AZ, UK.

<sup>‡</sup>Senior Lecturer, Department of Aeronautics, Imperial College London, London SW7 2AZ, UK.

<sup>§</sup>PhD student, Department of Aeronautics, Imperial College London, London SW7 2AZ, UK

<sup>¶</sup>Lecturer, Department of Aeronautics, Imperial College London, London SW7 2AZ, UK.

<sup>||</sup>Professor, Department of Aeronautics, Imperial College London, London SW7 2AZ, UK.

$\tilde{\mathcal{H}}^{\delta I}$	Tensor of the intercell numerical fluxes
<i>Subscripts</i>	
$i$	Inviscid
$v$	Viscous
$in$	inner
$BC$	Boundary condition state used to calculate the boundary numerical flux
$+$	Inner state (right)
$-$	Ghost state (left)

## I. Introduction

The implementation of boundary conditions (BCs) can have a significant impact on the overall accuracy of a numerical simulation especially when dealing with compressible flows, either inviscid or viscous. It is therefore important to implement them correctly in CFD solvers.

Usually BCs are imposed in two different ways: by directly modifying the boundary solution at each iteration/time-step (*strong* BCs) or by modifying the state from which the numerical flux is calculated<sup>a</sup> (*weak* BCs). Published studies to date suggest that weak BCs tend to improve convergence and can improve accuracy over strong BCs.<sup>1,7,8</sup> These studies are based upon steady simulations using predominantly low-order numerical methods, with successful application to high-order methods reported by Liu<sup>9</sup> and Bassi.<sup>3</sup>

In this paper we focus on a weak treatment of the BCs applied to the Euler and compressible Navier-Stokes equations within the context of compact discontinuous high-order spectral element methods (such as the discontinuous Galerkin (DG) method, and the high order Flux Reconstruction (FR) approach).

In the Euler equations and the advection term of the compressible Navier-Stokes equations, the weak BCs are implemented by defining a left and a right state in order to solve a Riemann problem at the boundary and calculate the boundary intercell numerical flux via a Riemann solver, either exact or approximated. In Fig. 1, the boundary is represented such that the external (ghost) state is on the right, and the solution internal space is on the left. The ghost state is used as the right state of the Riemann solver at the boundary. The convention in Nektar++ is that the normal vector at a boundary,  $\hat{\mathbf{n}}$ , is outwardly directed from the interior of the solution domain and the component of the velocity perpendicular to the boundary is  $V_n = \mathbf{V} \cdot \hat{\mathbf{n}}$ .

For Riemann invariant (characteristic), slip and no-slip conditions, we have adopted two different weak approaches. The first makes use of a Riemann solver, while the second directly calculate the intercell numerical flux at the given boundary by using the known solution. Hereafter we will refer to these two ways as Weak-Riemann and Weak-Prescribed approaches respectively.

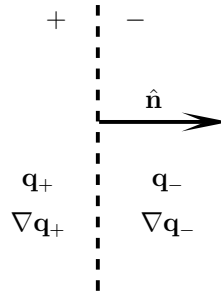


Figure 1. Nomenclature of the variables in proximity to a boundary

In the diffusion term of the compressible Navier-Stokes equations we used an LDG operator and the BCs are in this case applied in a *Weak-Prescribed* sense only.

To the knowledge of the authors, little work has been carried out to evaluate the influence of a *Weak-Prescribed* and a *Weak-Riemann* approach for applying slip and no-slip conditions. Finally, in the literature, there are no numerical comparisons which show the impact of different ghost states in the case of slip and no-slip BCs, an aspect which is also taken into account in the present work.

<sup>a</sup>Note that this is independent of the mathematical type of the BCs (Dirichlet, Neumann or Robin).

This paper is organised as follows. In Section 2, we show the governing equations being considered in the present work and their numerical discretisation within the context of compact discontinuous high-order spectral element methods. In particular we briefly describe the DG method and the FR approach.

In Section 3 we describe the implementation of BCs for the Euler equations. Specifically we consider Farfield (inflow/outflow) and slip BCs and we show the numerical results obtained in two simple test cases.

In Section 4 we highlight the implementation of BCs for the Navier-Stokes equations. We take into account Farfield / outflow conditions and no-slip conditions both isothermal and adiabatic. Also in this case we show some numerical results obtained on a flat-plate test case to show the effectiveness of the implementation.

In Section 5 we draw the overall picture and the main conclusions.

In Appendix A we describe three different Riemann solvers employed throughout our numerical results, an Exact Riemann solver, and two approximated Riemann solvers: HLL and HLLC.

All the numerical results are explained in detail to enable the reproducibility of all the test cases considered. We believe this aspect is particularly important, as it aims to provide a benchmark against which the BC implementation of any high-order CFD code can be tested. It also provides crucial insights into the effectiveness of some strategies relative to others.

## II. Governing equations

### A. Euler equations

#### 1. Overview

The Euler equations can be expressed as a hyperbolic conservation law in the form

$$\frac{\partial \mathbf{q}}{\partial t} + \frac{\partial \mathbf{f}_i}{\partial x} + \frac{\partial \mathbf{g}_i}{\partial y} + \frac{\partial \mathbf{h}_i}{\partial z} = 0, \quad (1)$$

where  $\mathbf{q}$  is the vector of the conserved variables,  $\mathbf{f}_i = \mathbf{f}_i(\mathbf{q})$ ,  $\mathbf{g}_i = \mathbf{g}_i(\mathbf{q})$  and  $\mathbf{h}_i = \mathbf{h}_i(\mathbf{q})$  are the vectors of the inviscid fluxes

$$\mathbf{q} = \begin{Bmatrix} \rho \\ \rho u \\ \rho v \\ \rho w \\ E \end{Bmatrix}, \quad \mathbf{f}_i = \begin{Bmatrix} \rho u \\ p + \rho u^2 \\ \rho uv \\ \rho uw \\ u(E + p) \end{Bmatrix}, \quad \mathbf{g}_i = \begin{Bmatrix} \rho v \\ \rho uv \\ p + \rho v^2 \\ \rho vw \\ v(E + p) \end{Bmatrix}, \quad \mathbf{h}_i = \begin{Bmatrix} \rho w \\ \rho vw \\ \rho vw \\ p + \rho w^2 \\ w(E + p) \end{Bmatrix}, \quad (2)$$

where  $\rho$  is the density,  $u$ ,  $v$  and  $w$  are the velocity components in  $x$ ,  $y$  and  $z$  directions,  $p$  is the pressure and  $E$  is the total energy. In this work we considered a perfect gas law for which the pressure is related to the total energy by the following expression

$$E = \frac{p}{\gamma - 1} + \frac{1}{2}\rho(u^2 + v^2 + w^2), \quad (3)$$

where  $\gamma$  is the ratio of specific heats.

#### 2. Numerical discretisation

The numerical framework for which the considerations on BCs have been imposed is part of the well-known family of discontinuous compact high-order numerical schemes. In this family of methods the computational domain  $\Omega$  is divided into  $N$  non-overlapping subdomains,  $\Omega \longrightarrow \Omega_n$ , and the solution is represented by a polynomial of degree  $\mathcal{P}$  within each element  $u_n \in \mathbb{P}^{\mathcal{P}}$ . The solution over the entire domain is allowed to be discontinuous between the elements. Therefore this class of methods is elemental-wise centred and the coupling between the elements is obtained through a boundary term which naturally arises from the variational formulation of this family of schemes.

We have used both DG and FR schemes in the attached study and will define which approach is adopted on a case by case basis.

### DG scheme :

The matrix form of the DG scheme applied to a general nonlinear hyperbolic system such as the Euler equations (2) is

$$\left. \frac{d\hat{\mathbf{q}}_n^\delta}{dt} \right|_\ell = \mathbf{M}^{-1} \left\{ \mathbf{S}_\xi \hat{\mathbf{f}}_{i_n}^\delta + \mathbf{S}_\eta \hat{\mathbf{g}}_{i_n}^\delta + \mathbf{S}_\zeta \hat{\mathbf{h}}_{i_n}^\delta - \tilde{\mathbf{b}}_{DG} \right\}_\ell \quad \text{for } \ell = 1, \dots, 5, \quad (4)$$

where  $\mathbf{M}$  is the elemental mass matrix,  $\mathbf{S}^\xi$ ,  $\mathbf{S}^\eta$  and  $\mathbf{S}^\zeta$  are the elemental advection matrices,  $\hat{\mathbf{f}}_{i_n}$ ,  $\hat{\mathbf{g}}_{i_n}$  and  $\hat{\mathbf{h}}_{i_n}$  are the elemental nonlinear fluxes of the Euler equations and finally  $\tilde{\mathbf{b}}_{DG}$  is the surface integral

$$\tilde{\mathbf{b}}_{DG} \Big|_\ell = \int_{\partial\Omega^n} \phi_{i,j,k} \left( \tilde{\mathcal{H}}_i^{\delta I} \cdot \mathbf{n}^f \right)_\ell ds \quad \text{for } \ell = 1, \dots, 5, \quad (5)$$

with  $\phi_{i,j,k}$  being a general polynomial expansion basis, either modal or nodal,  $\mathbf{n}^f$  being the outward normal of the face  $f$  of a given element  $\Omega_n$ , and  $\tilde{\mathcal{H}}_i^{\delta I}$  being the tensor of the inviscid fluxes  $\tilde{\mathcal{H}}_i^{\delta I} = [\hat{\mathbf{f}}_{i_n}^{\delta I}, \hat{\mathbf{g}}_{i_n}^{\delta I}, \hat{\mathbf{h}}_{i_n}^{\delta I}]$  at the boundary between two adjacent elements. For a more detailed discussion the interested reader can refer to Hesthaven and Warburton<sup>18</sup> or Karniadakis and Sherwin.<sup>19</sup>

### FR approach :

The matrix form of the FR approach is similar to that of the DG scheme with the exception that the FR approach does not involve the variational formulation of the equations but it takes into account the differential form

$$\left. \frac{d\hat{\mathbf{q}}_n^\delta}{dt} \right|_\ell = \left\{ \mathbf{D}_\xi \hat{\mathbf{f}}_{i_n}^{\delta D} + \mathbf{D}_\eta \hat{\mathbf{g}}_{i_n}^{\delta D} + \mathbf{D}_\zeta \hat{\mathbf{h}}_{i_n}^{\delta D} - \tilde{\mathbf{b}}_{FR} \right\}_\ell \quad \text{for } \ell = 1, \dots, 5, \quad (6)$$

where  $\mathbf{D}_\xi$ ,  $\mathbf{D}_\eta$  and  $\mathbf{D}_\zeta$  are the differentiation matrices with respect to  $\xi$ ,  $\eta$  and  $\zeta$  respectively,  $\hat{\mathbf{f}}_{i_n}$ ,  $\hat{\mathbf{g}}_{i_n}$  and  $\hat{\mathbf{h}}_{i_n}$  are the elemental nonlinear fluxes of Euler equations and  $\tilde{\mathbf{b}}_{FR}$  is the boundary term

$$\tilde{\mathbf{b}}_{FR} \Big|_\ell = \left( \tilde{\mathcal{H}}_i^{\delta C} \cdot \mathbf{n}^f \right)_\ell \Phi' = \left[ \left( \tilde{\mathcal{H}}_i^{\delta I} \cdot \mathbf{n}^f \right)_\ell - \left( \tilde{\mathcal{H}}_i^{\delta DI} \cdot \mathbf{n}^f \right)_\ell \right] \Phi' \quad \text{for } \ell = 1, \dots, 5, \quad (7)$$

with  $\Phi'$  being the derivative of a suitable correction function,  $\tilde{\mathcal{H}}_i^{\delta I}$  being the tensor of the inviscid fluxes  $\tilde{\mathcal{H}}_i^{\delta I} = [\hat{\mathbf{f}}_{i_n}^{\delta I}, \hat{\mathbf{g}}_{i_n}^{\delta I}, \hat{\mathbf{h}}_{i_n}^{\delta I}]$  at the boundary between two adjacent elements and  $\tilde{\mathcal{H}}_i^{\delta DI}$  being again the tensor of the inviscid fluxes evaluated at the boundary of a given element  $\Omega_n$ . For a more detailed and comprehensive discussion concerning the FR approach the interested reader can refer to Huynh<sup>15</sup> and to Vincent, Castonguay, and Jameson.<sup>16,17</sup>

One of the crucial features of both the methods and more in general of this class of schemes is the way the boundary term  $\tilde{\mathcal{H}}_i^{\delta I}$  is calculated. For the Euler equations and for the advection term of the compressible Navier-Stokes equations it is common to use either exact or approximated Riemann solvers. They both calculate an intermediate numerical flux at the interface between two adjacent elements by using some characteristic information coming from an eigenvalue analysis of the equations and may contain values coming from the left (+) or right (-) state of a given interface (see Fig. 1)

$$\tilde{\mathcal{H}}_i^{\delta I} \Big|_\ell = \tilde{\mathcal{H}}_i^{\delta I}(\hat{\mathbf{q}}_+, \hat{\mathbf{q}}_-) \Big|_\ell \quad \text{for } \ell = 1, \dots, 5. \quad (8)$$

Henceforth we omit the subscript “ $l$ ” for sake of clarity.

In this work we have considered an exact Riemann solver as well as two approximated Riemann solvers, HLL and HLLC, for which a detailed description and some implementative insights can be found in Appendix (A).

The boundary term  $\tilde{\mathcal{H}}_i^{\delta I}$  is also responsible for the BCs to be correctly transferred into the domain either via a ghost state as shown in Fig. 1 (Weak-Riemann approach) or via direct calculation of the boundary term using the known BCs (Weak-Prescribed approach). In the next Subsection we further explain the BCs treatment in case of Weak-Riemann and Weak-Prescribed approaches.

We want to remark here that the results obtained as part of this work hold true for this particular numerical framework independently on the particular discontinuous compact high-order approach adopted.

### 3. Treatment of the boundary conditions

As mentioned in the introduction we made use of two different approaches for applying the BCs. Both the approaches are weak in the sense that the BCs are applied to the fluxes rather than to the variables of the problem. The first approach consists in applying the BCs in an indirect manner through a Riemann solver whereas the second applies the BCs by calculating the fluxes directly from the known value of the variables at the boundary:

- *Weak-Riemann*:  $\tilde{\mathcal{H}}_i^{\delta I} = \tilde{\mathcal{H}}_i^{\delta I}(\hat{\mathbf{q}}_+^{\delta}, \hat{\mathbf{q}}_-^{\delta})$
- *Weak-Prescribed*:  $\tilde{\mathcal{H}}_i^{\delta I} = \tilde{\mathcal{H}}_i^{\delta I}(\hat{\mathbf{q}}_{BC}^{\delta})$

These two approaches are common in the family of methods considered in this paper and one implementation or the other depends on a series of factors which range from solver architecture, computational costs as well as robustness and effectiveness of the BCs implementation.

The *Weak-Riemann* approach is less intrusive with respect to the underlying numerics used at the inner interfaces of the numerical discretisation. On the other hand, the use of a Riemann solver for applying BCs implies the usage of a ghost point where it is necessary to apply a consistent ghost state which is not always trivial. Additionally, different Riemann solvers have different performance in transferring the BCs into the domain and one Riemann solver can perform better than another depending on the BCs being applied.

We additionally remark that another common way of applying the BCs is by setting directly the boundary solution, *strong* reinforcement, which is not taken into account in the present work.

## B. Navier-Stokes equations

### 1. Overview

The Navier-Stokes equations include the effects of fluid viscosity and heat conduction and are consequently composed by an inviscid and a viscous flux. They depend not only on the conserved variables but also, indirectly, on their gradient. The second order partial differential equations for the three-dimensional case can be written as:

$$\frac{\partial \mathbf{q}}{\partial t} + \frac{\partial \mathbf{f}}{\partial x} + \frac{\partial \mathbf{g}}{\partial y} + \frac{\partial \mathbf{h}}{\partial z} = 0, \quad (9)$$

where  $\mathbf{q}$  is the vector of the conserved variables,  $\mathbf{f} = \mathbf{f}(\mathbf{q}, \nabla(\mathbf{q}))$ ,  $\mathbf{g} = \mathbf{g}(\mathbf{q}, \nabla(\mathbf{q}))$  and  $\mathbf{h} = \mathbf{h}(\mathbf{q}, \nabla(\mathbf{q}))$  are the vectors of the fluxes which can also be written as:

$$\begin{aligned} \mathbf{f} &= \mathbf{f}_i - \mathbf{f}_v, \\ \mathbf{g} &= \mathbf{g}_i - \mathbf{g}_v, \\ \mathbf{h} &= \mathbf{h}_i - \mathbf{h}_v, \end{aligned} \quad (10)$$

where  $\mathbf{f}_i$ ,  $\mathbf{g}_i$  and  $\mathbf{h}_i$  are the inviscid fluxes of Eq. (2) and  $\mathbf{f}_v$ ,  $\mathbf{g}_v$  and  $\mathbf{h}_v$  are the viscous fluxes which take the following form:

$$\begin{aligned} \mathbf{f}_v &= \begin{Bmatrix} 0 \\ \tau_{xx} \\ \tau_{yx} \\ \tau_{zx} \\ u\tau_{xx} + v\tau_{yx} + w\tau_{zx} + kT_x \end{Bmatrix}, \quad \mathbf{g}_v = \begin{Bmatrix} 0 \\ \tau_{xy} \\ \tau_{yy} \\ \tau_{zy} \\ u\tau_{xy} + v\tau_{yy} + w\tau_{zy} + kT_y \end{Bmatrix}, \\ \mathbf{h}_v &= \begin{Bmatrix} 0 \\ \tau_{xz} \\ \tau_{yz} \\ \tau_{zz} \\ u\tau_{xz} + v\tau_{yz} + w\tau_{zz} + kT_z \end{Bmatrix}, \end{aligned} \quad (11)$$

where  $\tau_{xx}$ ,  $\tau_{xy}$ ,  $\tau_{xz}$ ,  $\tau_{yx}$ ,  $\tau_{yy}$ ,  $\tau_{yz}$ ,  $\tau_{zx}$ ,  $\tau_{zy}$  and  $\tau_{zz}$  are the components of the stress tensor<sup>b</sup>

$$\begin{aligned}\tau_{xx} &= 2\mu \left( u_x - \frac{u_x + v_y + w_z}{3} \right), & \tau_{yy} &= 2\mu \left( v_y - \frac{u_x + v_y + w_z}{3} \right), \\ \tau_{zz} &= 2\mu \left( w_z - \frac{u_x + v_y + w_z}{3} \right), & \tau_{xy} = \tau_{yx} &= \mu(v_x + u_y), \\ \tau_{yz} = \tau_{zy} &= \mu(w_y + v_z), & \tau_{zx} = \tau_{xz} &= \mu(u_z + w_x).\end{aligned}\tag{12}$$

where  $\mu$  is the dynamic viscosity calculated using the Sutherland's law and  $k$  is the thermal conductivity.

## 2. Numerical discretisation

The numerical discretisation of the compressible Navier-Stokes equations is equal to that of the Euler equations for the inviscid fluxes while the additional viscous fluxes are treated in a different manner. Specifically, to calculate the derivatives of the viscous fluxes one can split the procedure into two steps: the first step involves computing the spatial derivatives of the auxiliary variables  $\mathbf{q}_{aux} = [u, v, w, T]^T$ , the second step is to use these derivatives to compute the viscous fluxes. For both, DG and FR, the numerical fluxes at the interface between two adjacent elements are calculated without using a Riemann solver but using a different approach instead. In this work we made use of a local discontinuous Galerkin (LDG) method in which the numerical interface fluxes for the two steps above are computed as follows

$$\begin{aligned}\mathbf{q}_{aux}^{\delta I} &= \{\mathbf{q}_{aux}^{\delta}\} \pm \beta \cdot [\mathbf{q}_{aux}^{\delta}] \\ \mathcal{H}_v^{\delta I} &= \{\mathcal{H}_v^{\delta}\} \mp \beta \cdot [\tilde{\mathcal{H}}_v^{\delta}] - \gamma [\mathbf{q}_{aux}^{\delta}]\end{aligned}\tag{13}$$

where

$$\{\mathbf{g}\} = \frac{\mathbf{g}_+ + \mathbf{g}_-}{2}, \quad [\mathbf{g}] = \frac{\mathbf{g}_+ \mathbf{n}_+ + \mathbf{g}_- \mathbf{n}_-}{2}, \quad \beta = \frac{1}{2} \mathbf{n}_+\tag{14}$$

with the quantities  $\mathbf{g}_-$  and  $\mathbf{g}_+$  being the variable  $\mathbf{g}$  on the right and on the left side of the interface between two elements and with  $\mathbf{n}_+$  and  $\mathbf{n}_-$  being the respective normals (for additional details the interested reader can refer to Cockburn and Shu<sup>4</sup>). Other choices for computing the interface fluxes can be adopted such as the interior penalty (IP) method (see Arnold<sup>6</sup>), the compact DG (CDG) method (see Peraire and Persson,<sup>5</sup> the central flux (CF) and the second Bassi-Rebay method (BR2) (see Bassi and Rebay<sup>3</sup>). It can be observed that the interface fluxes, as defined in Eq. (13), can recover the CF and the BR2 methods for different choices of  $\beta$ .

As for the case of the inviscid flux, where the boundary term (i.e. the interface flux) transfers the BCs into the domain, for the viscous flux the interface fluxes of the auxiliary variables  $\mathbf{q}_{aux}^{\delta I}$  and of the primitive system  $\tilde{\mathcal{H}}^{\delta I}$  are responsible for the BCs to be correctly transferred into the domain. In this case, due to the flip-flop nature of the LDG approach, the BCs are applied in a Weak-Prescribed sense and in particular, where the solution is known we directly apply this solution to calculate the corresponding flux whereas if the solution is unknown we extrapolate the solution from the interior point.

## III. BCs for Compressible Euler equations

For the compressible Euler equations we consider two types of BC.

- Farfield BCs: in this section we study both the *Weak-Riemann* approach and the *Weak-Prescribed* approach. Regarding the second approach we take into account two ways for applying the BCs, *Riemann invariant* and  *$\infty$ -value*. In the first way the conditions are applied by combining the information which travels on the incoming and outgoing characteristic waves. In the second way, at the boundary, the free-stream conditions are applied without considering the internal state. We show how this approach leads to the divergence of the simulation since it does not account for the hyperbolicity of the problem.
- Slip BCs: in this section we thoroughly compare the *Weak-Riemann* and the *Weak-Prescribed* approaches. Specifically in case of *Weak-Riemann* approach we consider two methodologies. We explain why, using a Riemann solver, the first methodology is the correct way to impose the BCs whilst the second is suboptimal.

<sup>b</sup>In the Navier-Stokes equations for all the simulations it was used the Stokes hypothesis  $\lambda = -2/3$ .

In the following all the equations are written in their dimensional form, the free-stream values are denoted by the subscript  $\infty$  and the values from the interior by the subscript *in* (not to be confused with inviscid).

## A. Farfield BCs

### 1. Overview

Farfield BCs for the Euler equations have been widely explored in the past decades and the interested reader can refer to Thompson<sup>12,13</sup> and Giles.<sup>14</sup> In this Section we describe a characteristic approach based on the Riemann solver and a Riemann invariant approach.

According to the hyperbolic nature of the Euler equations the flux evaluated at the boundary is a combination of the information coming from inside and outside the domain. We take into consideration two ways for applying the BCs. The first is a *Weak-Riemann* approach and the second is a *Weak-Prescribed* approach.

- *Weak-Riemann  $\infty$ -value*: All the variables at the boundary are specified from free-stream conditions. The complete ghost state is:

$$\mathbf{q}_- = \begin{Bmatrix} \rho_- \\ (\rho u)_- \\ (\rho v)_- \\ (\rho w)_- \\ E_- \end{Bmatrix} = \begin{Bmatrix} \rho_\infty \\ \rho_\infty u_\infty \\ \rho_\infty v_\infty \\ \rho_\infty w_\infty \\ E_\infty \end{Bmatrix}. \quad (15)$$

and the flux is then calculated by a Riemann solver as follows

$$\tilde{\mathcal{H}}_i^I = \tilde{\mathcal{H}}_i^I(\hat{\mathbf{q}}_+, \hat{\mathbf{q}}_-), \quad (16)$$

where  $\hat{\mathbf{q}}_+$  and  $\hat{\mathbf{q}}_-$  are the inner and the ghost state respectively. In evaluating the boundary flux the Riemann solver takes automatically into account the eigenvalues (characteristic lines) of the Euler equations and therefore the problem is always well posed.

- *Weak-Prescribed*: We compute the boundary flux directly from a known solution. We distinguish the following two cases (the second is mathematically inconsistent and therefore wrong).

#### *Riemann invariant*

The Riemann invariants are associated with the incoming  $R_-$  and outgoing  $R_+$  characteristic waves. We have to identify if the sign of  $V_n$  is positive (outflow) or negative (inflow) at the boundary.

#### **Inflow**

In the case of an inflow region the incoming Riemann invariant uses the  $\infty$ -value condition  $\mathbf{q}_\infty = [\rho_\infty, (\rho u)_\infty, (\rho v)_\infty, (\rho w)_\infty, E_\infty]^T$ , while the outgoing Riemann invariant uses the condition from the interior of the domain  $\mathbf{q}_{in} = [\rho_{in}, (\rho u)_{in}, (\rho v)_{in}, (\rho w)_{in}, E_{in}]^T$ . So the appropriate Riemann invariants to consistently solve the hyperbolic problem are:

$$R_+ = V_{in} + \frac{2c_{in}}{\gamma - 1}, \quad R_- = V_\infty - \frac{2c_\infty}{\gamma - 1} \quad (17)$$

where:

$$V_{in} = \mathbf{V}_{in} \cdot \hat{\mathbf{n}}, \quad V_\infty = \mathbf{V}_\infty \cdot \hat{\mathbf{n}}, \quad c_{in}^2 = \frac{\gamma p_{in}}{\rho_{in}}, \quad c_\infty^2 = \frac{\gamma p_\infty}{\rho_\infty} \quad (18)$$

with  $\mathbf{V}_{in} = [u_{in}, v_{in}, w_{in}]^T$  and  $\mathbf{V}_\infty = [u_\infty, v_\infty, w_\infty]^T$ .



If the flow at the boundary point is supersonic,  $M_{in} = |V_{in}|/c_{in} \geq 1$ , there is no outgoing characteristic wave and  $R_+$  is set as:

$$R_+ = U_\infty + \frac{2c_\infty}{\gamma - 1}. \quad (19)$$

In addition we know that

$$R_{+,b} = V_b + \frac{2c_b}{\gamma - 1} = R_+, \quad R_{-,b} = V_b - \frac{2c_b}{\gamma - 1} = R_-. \quad (20)$$

From Eq. (20) we can therefore calculate a velocity and a speed of sound at the boundary as follows:

$$V_b = \frac{R_+ + R_-}{2}, \quad c_b = \frac{(\gamma - 1)(R_+ - R_-)}{4}. \quad (21)$$

The velocity  $V_b$  can then be used to calculate the physical velocity at the boundary:

$$\mathbf{V}_b = \mathbf{V}_\infty + (V_b - \mathbf{V}_\infty \cdot \hat{\mathbf{n}})\hat{\mathbf{n}}. \quad (22)$$

where  $\mathbf{V}_b = [u_b, v_b, w_b]^T$ .

Since the flow is entering the domain the entropy at the boundary is equal to the free-stream entropy:

$$s_b = \frac{c_\infty^2}{\gamma \rho_\infty^{\gamma-1}}. \quad (23)$$

The density and the pressure at the boundary can be calculated as:

$$\rho_b = \left( \frac{c_b^2}{\gamma s_b} \right), \quad p_b = \frac{\rho_b c_b^2}{\gamma}. \quad (24)$$

It is then possible to calculate the energy  $E_b$  from Eq. (3) and all the conserved variables can be evaluated:

$$\mathbf{q}_{BC} = \begin{Bmatrix} \rho_{BC} \\ (\rho u)_{BC} \\ (\rho v)_{BC} \\ (\rho w)_{BC} \\ E_{BC} \end{Bmatrix} = \begin{Bmatrix} \rho_b \\ \rho_b u_b \\ \rho_b v_b \\ \rho_b w_b \\ E_b \end{Bmatrix}. \quad (25)$$

Eq. (25) is used to calculate the boundary intercell numerical flux as follows boundary flux becomes

$$\tilde{\mathcal{H}}_i^I = \tilde{\mathcal{H}}_i^I(\hat{\mathbf{q}}_{BC}). \quad (26)$$

## Outflow

In the case of an outflow region the Riemann invariants are the same of Eq. (17). If the flow at the boundary point is supersonic,  $M_{in} = |V_{in}|/c_{in} \geq 1$ , there is no incoming characteristic wave and  $R^-$  is set as:

$$R_- = U_{in} - \frac{2c_{in}}{\gamma - 1} \quad (27)$$

At the boundary the velocity  $V_b$  and the speed of sound  $c_b$  can be calculated as in Eq. (21). The velocity  $V_b$  can then be used to calculate the physical velocity at the boundary:

$$\mathbf{V}_b = \mathbf{V}_{in} + (V_b - \mathbf{V}_{in} \cdot \hat{\mathbf{n}})\hat{\mathbf{n}} \quad (28)$$

where  $\mathbf{V}_b = [u_b, v_b, w_b]^T$ . Since the flow is exiting the domain the entropy at the boundary is extrapolated from the interior and is equal to:

$$s_b = \frac{c_{in}^2}{\gamma \rho_{in}^{\gamma-1}}. \quad (29)$$

The density and the pressure at the boundary can be calculated with Eq. (24). Therefore we can evaluate all the conserved variables as in Eq. (25). The flux is then evaluated as in Eq. (26)

$\infty$ -value: We compute the flux directly from the free-stream solution:

$$\mathbf{q}_{BC} = \begin{Bmatrix} \rho_{BC} \\ (\rho u)_{BC} \\ (\rho v)_{BC} \\ (\rho w)_{BC} \\ E_{BC} \end{Bmatrix} = \begin{Bmatrix} \rho_{\infty} \\ \rho_{\infty} u_{\infty} \\ \rho_{\infty} v_{\infty} \\ \rho_{\infty} w_{\infty} \\ E_{\infty} \end{Bmatrix} \quad (30)$$

using Eq. (26).

This last methodology is incorrect since we are not considering the sign of the eigenvalues at the boundary and, so, the problem is not well posed. The only way to correctly apply the farfield BCs through a *Weak-Prescribed* approach is to use the *Riemann invariant* (characteristic) methodology. In fact, in the results shown in the next Subsection, it can be seen that the characteristic treatment of the farfield boundary recovers exactly the *Weak-Riemann* approach where the ghost state in Eq. (15) is used in conjunction with an exact Riemann solver. In this case, the Riemann solver takes automatically into account the sign of the eigenvalues and evaluates the flux by combining the inner and outer state.

## 2. Numerical results

We tested the Farfield BCs using a 2D problem where a perturbation on the initial pressure and density fields generated a system of characteristic waves travelling towards the boundaries. The initial condition was

$$\begin{cases} \rho(\mathbf{x}, t = 0) = \rho_{\infty}(1 + A e^{\frac{-(x^2+y^2)}{2\sigma^2}}) \\ \rho u(\mathbf{x}, t = 0) = \rho u_{\infty} \\ \rho v(\mathbf{x}, t = 0) = \rho v_{\infty} \\ E(\mathbf{x}, t = 0) = \frac{p_{\infty}}{\gamma - 1}(1 + A e^{\frac{-(x^2+y^2)}{2\sigma^2}}) + \frac{1}{2}\rho(u_{\infty}^2 + v_{\infty}^2), \end{cases} \quad (31)$$

where  $\sigma = 0.002$ .

Simulations of both subsonic and supersonic test cases were performed, with  $M_{\infty} = 0.5$  for the subsonic case, and  $M_{\infty} = 1.5$  for the supersonic case. Both the FR approach and the DG method were used. The temporal discretisation applied was a 4<sup>th</sup> order Runge-Kutta scheme.

The main aim of the numerical simulations was to demonstrate the effectiveness of the BCs within a comprehensive high-order numerical context, and provide a possible benchmark to test the implementation of BCs in any high-order CFD code.

The objective of the Riemann invariant is to minimise wave reflections from the boundary. We therefore measured the following parameter as a quantitative indicator of the effectiveness of each implementation:

$$r = \frac{A_{incident}}{A_{reflected}}. \quad (32)$$

The reflection parameter  $r$  was computed using the incident wave amplitude  $A_{incident}$  at  $t = 0.00027 s$  (shown in Fig. 2(a)) and the reflection wave amplitude  $A_{reflected}$  at  $t = 0.00032 s$  (shown in Fig. 2(b)) for all the subsonic cases. Table 1 shows also that the approximated solvers provide similar results to the exact Riemann solver — if the  $\infty$  quantities are used in the ghost state. However, the difference seen when using a purely average of the inner and outer values is remarkable. A reflected wave of much greater amplitude is produced. This is because the average procedure does not take into account how information travel on the characteristic lines and, so, should not be used.

The data for the supersonic case are not shown because they provided a zero-reflection for all the cases except for the *Weak-Prescribed* approach in conjunction with  $\infty$ -values which made the simulation diverge.

The use of an exact Riemann solver at the boundary is equivalent to employing explicitly Riemann invariant BCs. This is also evident from the results shown in Table 1, where the application of a *Weak-Prescribed Riemann invariant* approach, and the application of the *Weak-Riemann  $\infty$ -values* approach gives

Table 1. Parameter  $r$  as a function of the polynomial order and of the flux technique used at the boundary: Subsonic case,  $M_\infty = 0.5$  ( $A = 0.01$ ).

	$r[\%], \mathcal{P} = 5$	$r[\%], \mathcal{P} = 7$	$r[\%], \mathcal{P} = 9$	$r[\%], \mathcal{P} = 11$
<b>Weak-Riemann Exact</b> - $\infty$	0.4909	0.5260	0.5260	0.5325
<b>Weak-Riemann HLLC</b> - $\infty$	0.4909	0.5260	0.5260	0.5325
<b>Weak-Riemann HLL</b> - $\infty$	0.4909	0.5260	0.5260	0.5325
<b>Weak-Riemann Average</b> - $\infty$	7.8538	8.4849	13.7441	22.6147
<b>Weak-Prescribed</b> - RI	0.4909	0.5260	0.5260	0.5325
<b>Weak-Prescribed</b> - $\infty$	Diverged	Diverged	Diverged	Diverged

Table 2. Parameter  $r$  as a function of the amplitude  $A$  of the perturbation and of the flux technique used at the boundary: Subsonic case,  $M_\infty = 0.5$  ( $P = 5$ ).

	$r[\%], A = 0.01$	$r[\%], A = 0.1$	$r[\%], A = 1$
<b>Weak-Riemann Exact</b> - $\infty$	0.4909	0.4801	0.4249
<b>Weak-Prescribed</b> - RI	0.4909	0.4801	0.4249
<b>Weak-Prescribed</b> - $\infty$	diverged	diverged	diverged

identical results. It is evident that there is no dependence on the polynomial order; the incident and reflected waves were therefore completely resolved for all polynomial orders. The use of a *Weak-Prescribed*  $\infty$ -values approach (last row of Table 1) leads to divergence as expected.

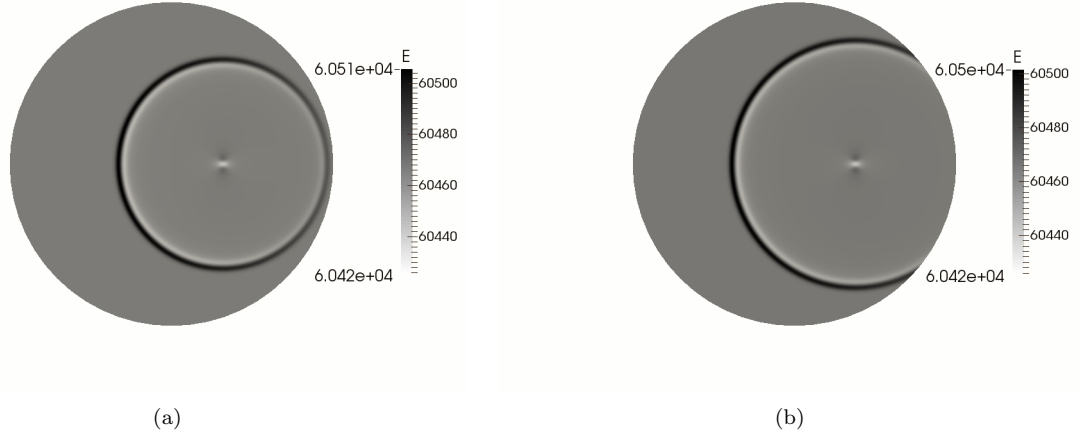


Figure 2. Energy contour at  $t = 27s$  (a) and  $t = 32s$  (b).

Similar experiments were performed by varying the amplitude of the perturbation  $A = [0.01, 0.1, 1]$ . Table 2 shows the results obtained using a fifth-order polynomial and both a Weak-Riemann and a Weak-Prescribed evaluation of the flux function. We can see how the reflection parameter  $r$  is not influenced by the amplitude of the perturbation.

## B. Slip Wall BCs

### 1. Overview

For the Euler equations, the boundary condition must prevent the fluid from penetrating the wall. We consider a *Weak-Riemann* approach and a *Weak-Prescribed* approach.

- *Weak-Riemann*: We use two different ways for applying a slip condition on the advection term.

A1: The first choice is to evaluate the interior velocity field at the boundary  $\mathbf{V}_{in} = [u_{in}, v_{in}, w_{in}]^T$  and then calculate  $\mathbf{V}_- = [u_-, v_-, w_-]^T$  as:

$$\mathbf{V}_- = \mathbf{V}_{in} - 2(\mathbf{V}_{in} \cdot \hat{\mathbf{n}})\hat{\mathbf{n}} \quad (33)$$

This is equivalent to imposing the same tangential component in the ghost point as in the interior,  $V_{-,t} = V_{in,t} = V_{+,t}$ , and an opposite normal component of the velocity,  $V_{-,n} = -V_{in,n} = -V_{+,n}$ , where the subscript  $t$  denotes the tangential direction and the subscript  $n$  denotes the normal direction.

The density and internal energy are extrapolated from the interior such that the complete ghost state is

$$\mathbf{q}_- = \begin{Bmatrix} \rho_- \\ (\rho u)_- \\ (\rho v)_- \\ (\rho w)_- \\ E_- \end{Bmatrix} = \begin{Bmatrix} \rho_{in} \\ \rho_{in}u_{in} - 2(\mathbf{V}_{in} \cdot \hat{\mathbf{n}})\hat{n}_x \\ \rho_{in}v_{in} - 2(\mathbf{V}_{in} \cdot \hat{\mathbf{n}})\hat{n}_y \\ \rho_{in}w_{in} - 2(\mathbf{V}_{in} \cdot \hat{\mathbf{n}})\hat{n}_z \\ E_{in} \end{Bmatrix} \quad (34)$$

and the boundary flux is calculated through a Riemann solver as

$$\tilde{\mathcal{H}}_i^I = \tilde{\mathcal{H}}_i^I(\hat{\mathbf{q}}_+, \hat{\mathbf{q}}_-), \quad (35)$$

where  $\hat{\mathbf{q}}_+$  and  $\hat{\mathbf{q}}_-$  are the inner and the ghost state respectively.

The normal component of the velocity evaluated by the Riemann solver is zero since the only non-zero contributions to the flux function are those coming from the pressure in the momentum equations.

A2: The second choice considered is to set the ghost normal velocity to zero instead of negating it such that the complete ghost state is

$$\mathbf{q}_- = \begin{Bmatrix} \rho_- \\ (\rho u)_- \\ (\rho v)_- \\ (\rho w)_- \\ E_- \end{Bmatrix} = \begin{Bmatrix} \rho_{in} \\ \rho_{in}u_{in} - (\mathbf{V}_{in} \cdot \hat{\mathbf{n}})\hat{n}_x \\ \rho_{in}v_{in} - (\mathbf{V}_{in} \cdot \hat{\mathbf{n}})\hat{n}_y \\ \rho_{in}w_{in} - (\mathbf{V}_{in} \cdot \hat{\mathbf{n}})\hat{n}_z \\ \frac{p_{in}}{\gamma-1} + \frac{1}{2}\rho_{in}V_{in,t}^2 \end{Bmatrix} \quad (36)$$

and the boundary flux is calculated through a Riemann solver as in Eq. (35).

With this boundary condition the Riemann solver calculates an intermediate state where the normal component of the velocity is non-zero. This causes an unphysical behaviour with non-zero numerical mass and energy fluxes passing through the wall. For this reason this methodology is not appropriate.

- *Weak-Prescribed*: In this case we by-pass the Riemann solver at the boundary and we compute the boundary flux directly from the known solution

$$\mathbf{q}_{BC} = \begin{Bmatrix} \rho_{BC} \\ (\rho u)_{BC} \\ (\rho v)_{BC} \\ (\rho w)_{BC} \\ E_{BC} \end{Bmatrix} = \begin{Bmatrix} \rho_{in} \\ \rho_{in}u_{in} - (\mathbf{V}_{in} \cdot \hat{\mathbf{n}})\hat{n}_x \\ \rho_{in}v_{in} - (\mathbf{V}_{in} \cdot \hat{\mathbf{n}})\hat{n}_y \\ \rho_{in}w_{in} - (\mathbf{V}_{in} \cdot \hat{\mathbf{n}})\hat{n}_z \\ \frac{p_{in}}{\gamma-1} + \frac{1}{2}\rho_{in}V_{in,t}^2 \end{Bmatrix} \quad (37)$$

and the boundary flux becomes

$$\tilde{\mathcal{H}}_i^I = \tilde{\mathcal{H}}_i^I(\hat{\mathbf{q}}_{BC}). \quad (38)$$

## 2. Numerical results

For testing the various types of slip BCs described above we used the cylinder mesh in Fig. 3 composed by  $160 \times 29$  elements. As farfield BCs we employed Eq. (15) in conjunction with an exact Riemann solver.

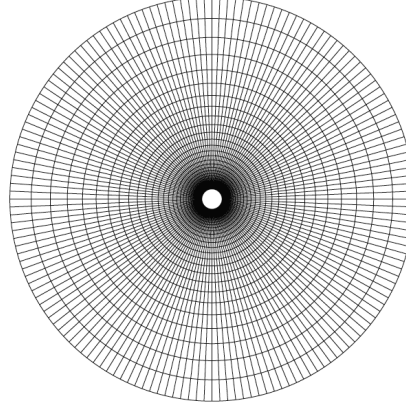


Figure 3. Grid used for the slip BCs experiments.

For all the simulations we used a subsonic Mach number  $M_\infty = 0.1$ . The time-integration scheme employed was a two-stage Runge-Kutta and we used the FR scheme. We used three different polynomial orders,  $\mathcal{P} = 2, 4, 6$ . The approaches taken into consideration were a Weak-Prescribed (Eq. (37)) and the two different Weak-Riemann approaches, *Weak-Riemann-A1* (Eq. (34)) and *Weak-Riemann-A2* (Eq. (36)). We used the exact Riemann solver for both the approaches except at the slip boundary region in the case of Weak-Prescribed.

Table 3. Normal velocity  $V_n$  at the wall as a function of the polynomial order and of the flux technique used at the boundary: slip BCs

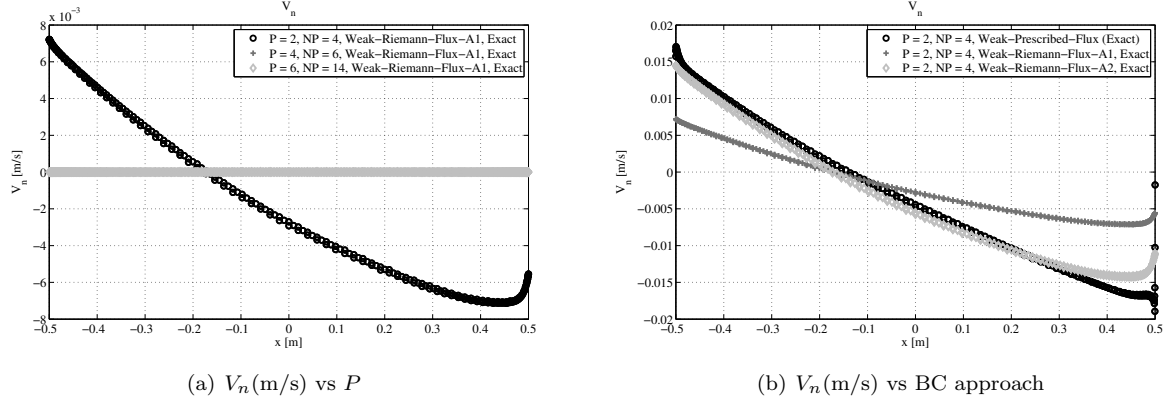
	$V_n[m/s], \mathcal{P} = 2$	$V_n[m/s], \mathcal{P} = 4$	$V_n[m/s], \mathcal{P} = 6$
<b>Weak-Riemann-A1</b>	$4.816 \times 10^{-3}$	$4.362 \times 10^{-6}$	aliasing ( $1.641 \times 10^{-7}$ )
<b>Weak-Riemann-A2</b>	$9.644 \times 10^{-3}$	aliasing ( $-3.495 \times 10^{-6}$ )	aliasing ( - )
<b>Weak-Prescribed</b>	$1.060 \times 10^{-2}$	$-3.770 \times 10^{-6}$	aliasing ( - )

Table 4. Lift and drag force as a function of the polynomial order and of the flux technique used at the boundary: slip BCs

	$ \mathbf{L} - \mathbf{L}_{exact} [N]$		
	$\mathcal{P} = 2$	$\mathcal{P} = 4$	$\mathcal{P} = 6$
<b>Weak-Riemann-A1</b>	$2.368 \times 10^{-6}$	$2.894 \times 10^{-6}$	aliasing ( $3.723 \times 10^{-7}$ )
<b>Weak-Riemann-A2</b>	$-1.183 \times 10^{-6}$	aliasing ( $7.246 \times 10^{-7}$ )	aliasing ( - )
<b>Weak-Prescribed</b>	$-2.342 \times 10^{-5}$	$9.730 \times 10^{-8}$	aliasing ( - )
	$ \mathbf{D} - \mathbf{D}_{exact} [N]$		
	$\mathcal{P} = 2$	$\mathcal{P} = 4$	$\mathcal{P} = 6$
<b>Weak-Riemann-A1</b>	-1.158	$2.304 \times 10^{-2}$	aliasing ( $2.397 \times 10^{-2}$ )
<b>Weak-Riemann-A2</b>	-1.133	aliasing ( $2.303 \times 10^{-2}$ )	aliasing ( - )
<b>Weak-Prescribed</b>	$2.514 \times 10^{-2}$	$2.397 \times 10^{-2}$	aliasing ( - )

For the evaluation of the slip conditions we study the convergence to steady-state and we compare three quantities at the wall, namely lift  $L$ , drag  $D$  and normal velocity  $V_n$ .

For both the configurations, Weak-Riemann and Weak-Prescribed, we used a time-step such that the error due to the time-stepping was negligible. In Table 3 we show the average of the absolute values of the normal velocity  $V_n$  over the cylinder wall, as functions of the polynomial order  $P$  and of the type of BCs applied. The Weak-Riemann-A1 approach provides the best results both in terms of accuracy and robustness. The other approaches, especially the Weak-Riemann-A2 were influenced by large aliasing issues. The errors of the surface forces, lift and drag, are shown in Table 4 again as function of the polynomial order and of the BC approach adopted.



**Figure 4.** Comparison of wall normal velocities  $V_n$  by varying the polynomial order [4(a)] and by varying the BC approach for  $P = 2$  [4(b)]

In the calculations performed, the Weak-Riemann-A1 approach showed to be the most robust. The Weak-Riemann-A2 and the Weak-Prescribed were affected by aliasing issues which made the simulations diverge for high polynomial orders if inexact quadrature was used. If we consider the error of the normal velocity, the Weak-Riemann-A1 has the best accuracy. Specifically the errors of  $V_n$  with the Weak-Riemann-A2 and Weak-Prescribed are very similar and are twice the error with respect to the Weak-Riemann-A1 (see Table 3). The difference between the two Weak-Riemann approaches is theoretically clear and associated with the nature of the Riemann problem being solved at the boundary: If we apply as ghost state the same thermodynamic quantities as the inner state and we also guarantee that the ghost velocity is the opposite (in sign) of the inner velocity, then the Riemann problem being solved at the boundary has a contact wave located at  $x/t = 0$  (i.e.  $u_* = 0$ ) and therefore the only possible solutions are within the region between the two nonlinear waves (star region). Since the solution in the star region is calculated with the star values of pressure and velocity,  $p_*$  and  $u_*$  through Riemann invariants or Rankine-Hugoniot relations, the fluxes associated with the mass and the energy are zero whilst the momentum fluxes have the contributions of the star pressure  $p_*$  and of the tangential velocity. The behaviour of the Weak-Prescribed approach is instead not obvious. With regard to the errors in the forces over the surface the evaluations undertaken are influenced by aliasing issues and, hence, are not a good indicator of the type of BCs to be applied.

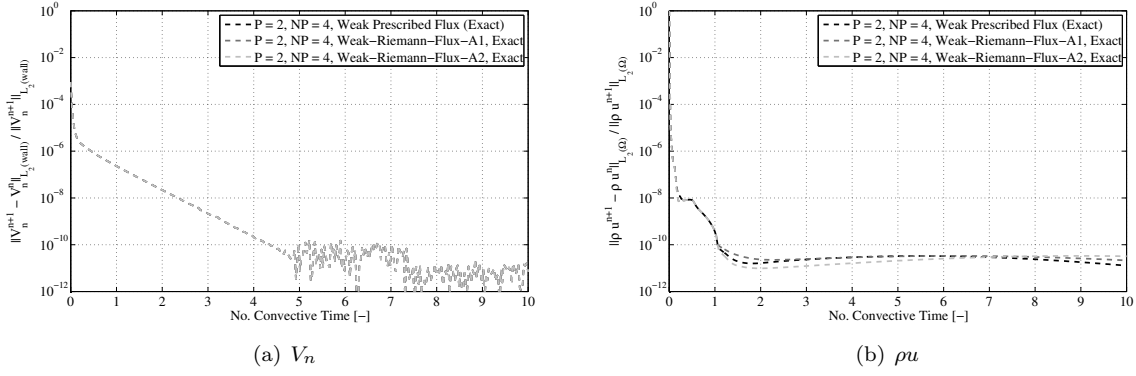


**Figure 5.** Convergence history of the  $V_n$  residual at the wall [5(a)] and convergence history of the  $\rho u$  residual for the entire domain [5(b)] in the cases of Weak-Prescribed BCs (black dashed line), Weak-Riemann-A1 BCs (grey dashed line) and Weak-Riemann-A2 BCs (light grey dashed line)

Finally considering the convergence to steady-state, in Fig. 5 we show the convergence history of  $V_n$  at the wall (Fig. 5(a)) and the convergence history of  $\rho u$  for the entire domain (Fig. 5(b)). The convergence of the wall is slower than the convergence of the entire domain and no significant differences can be seen between the various BC approaches used, especially for the convergence of the normal velocity at the wall which is identical in all the approaches.

## IV. BCs for Compressible Navier-Stokes equations

For the compressible Navier-Stokes equations we consider two BC typologies.

- Farfield and outflow BCs: in this section we show how it is possible to implement an outflow BC which can take into account steady (laminar) viscous effects (e.g. outflow region of a flat-plate). In addition we highlight when the Riemann invariant BCs presented for the Euler equations can be effectively used in the context of the Navier-Stokes equations. In this case we explore only the *Weak-Riemann* imposition with no mention to the *Weak-Prescribed* approach.
- No-slip BCs: in this section we thoroughly compare the *Weak-Riemann* and the *Weak-Prescribed* approaches. As for the slip BCs case, for the *Weak-Riemann* approach we consider two methodologies, *A1* and *A2*. We explain why, using a Riemann solver, the first methodology is the correct way to impose the BCs whilst the second is wrong.

### A. Farfield and outflow BCs

#### 1. Overview

Farfield and outflow BCs for the compressible Navier-Stokes equations are still a very active topic of research. While for the Euler equations a characteristic approach based on the eigenvalue analysis of the advection operator works effectively, for the Navier-Stokes equations such an approach provides spurious reflections when vortical structures (e.g. shedding behind an object, turbo machinery wakes, etc.) passes through the boundary.

The aim of this section is to describe when we can apply the characteristic approach presented for the Euler equations and what we can do to take into account steady (laminar) viscous effects.

The case of turbulence and vortical structures passing through a farfield/outflow boundary is not taken into consideration since it is out of the scope of the present work. Related to this topic, the interested reader can refer to Poinot and Lele,<sup>11</sup> Colonius,<sup>21</sup> Moin,<sup>22</sup> Mani,<sup>23</sup> Lodato<sup>10</sup> and Pirozzoli.<sup>24</sup>

The model problem is either a subsonic or a supersonic flow past a flat-plate with a developing boundary-layer. The questions are:

- How can we apply an effective BCs at the outflow without interfering with the boundary-layer development?

- Can we make such a BCs non-reflective at least in terms of the acoustic mode (possibly recovering the same performance of the Characteristic BCs presented for the Euler equations)?

The application of Characteristic BCs (equivalently applying a ghost state equal to the  $\infty$  state and using an exact Riemann solver) presented for the Euler equations works properly in regions where viscosity effects can be neglected. If we consider for instance our model problem, effective regions where this BCs works very well are the top boundary and the inflow. In these regions the viscous effects are negligible and the only reflection we need to prevent is an acoustic reflection. In the results section we show that the application of this condition provides excellent results in terms of minimising the acoustic reflections.

On the other hand, the application of the same BCs at the outflow is incorrect since it provides an unphysical solution because the velocity is constrained by the characteristic information prescribed at the boundary. To appropriately recover the physical solution (i.e. a developing boundary layer) we need to leave the velocity free. This feature is typically achieved by assigning to the ghost state the inner state (also known as do-nothing approach) in the case of supersonic regime or by applying a pressure outflow boundary condition in the case of subsonic regime.

For this BCs we show a *Weak-Riemann* approach only.

### Advection term

We treat the advection term in a *Weak-Riemann* fashion only and we distinguish two different implementations.

- Reflective pressure outflow (R): the pressure assumes the value of an estimated or exact outer state denoted with  $(p_e)$  if the flow is subsonic:

$$\mathbf{q}_- = \begin{pmatrix} \rho_- \\ (\rho u)_- \\ (\rho v)_- \\ (\rho w)_- \\ E_- \end{pmatrix} = \begin{pmatrix} \rho_{in} \\ \rho_{in} u_{in} \\ \rho_{in} v_{in} \\ \rho_{in} w_{in} \\ \frac{p_e}{\gamma-1} + \frac{1}{2} \rho_{in} (u_{in}^2 + v_{in}^2 + w_{in}^2) \end{pmatrix}. \quad (39)$$

Otherwise we extrapolate the entire ghost state from the interior values:

$$\mathbf{q}_- = \begin{pmatrix} \rho_- \\ (\rho u)_- \\ (\rho v)_- \\ (\rho w)_- \\ E_- \end{pmatrix} = \begin{pmatrix} \rho_{in} \\ \rho_{in} u_{in} \\ \rho_{in} v_{in} \\ \rho_{in} w_{in} \\ \frac{p_{in}}{\gamma-1} + \frac{1}{2} \rho_{in} (u_{in}^2 + v_{in}^2 + w_{in}^2) \end{pmatrix}. \quad (40)$$

- Partially non-reflective pressure outflow (PNR): in this case the pressure is the difference between two times an estimated or exact outer state denoted with  $(p_e)$  and the inner pressure  $(p_{in})$  if the flow is subsonic:

$$\mathbf{q}_- = \begin{pmatrix} \rho_- \\ (\rho u)_- \\ (\rho v)_- \\ (\rho w)_- \\ E_- \end{pmatrix} = \begin{pmatrix} \rho_{in} \\ \rho_{in} u_{in} \\ \rho_{in} v_{in} \\ \rho_{in} w_{in} \\ \frac{2p_e - p_{in}}{\gamma-1} + \frac{1}{2} \rho_{in} (u_{in}^2 + v_{in}^2 + w_{in}^2) \end{pmatrix}. \quad (41)$$

Otherwise we reuse Eq. (40).

The first implementation is called reflective since it gives rise to spurious oscillations of pressure at the boundary which may affect the overall solution of the problem whereas the second is called partially non-reflective since the spurious oscillations at the boundary are damped in time leading to a convergent, despite slow, solution.

It should be also noted that either approaches can be used for all the simulations where a good pressure estimate at the outflow is known a priori. This can be either obtained analytically whether possible or numerically by solving the Euler equations when we can assume  $\frac{\partial p}{\partial n} = 0$ .



## Diffusion term

For the diffusion term of the compressible Navier-Stokes equations, the auxiliary variables  $\mathbf{q}_{aux}$ , which are used to calculate the first order derivatives, need to be imposed at the boundary. Since we are using an LDG approach we directly impose the values of the auxiliary variables at the boundary in a Weak-Prescribed fashion due to the flip-flop nature of the LDG approach. It should be noted however that by using a different approach such as the CF, the IP or the BR2 approaches this imposition can be different. For instance, in the case of CF approach, the diffusion flux is an average between the inner and the ghost state.

Focusing on the LDG approach, in the case of an *outflow* / *farfield* boundary, the auxiliary variables are

$$\mathbf{q}_{aux_{BC}} = \begin{Bmatrix} u_{BC} \\ v_{BC} \\ w_{BC} \\ T_{BC} \end{Bmatrix} = \begin{Bmatrix} u_{in} \\ v_{in} \\ w_{in} \\ \frac{p_{in}}{\rho_{in} R} \end{Bmatrix}. \quad (42)$$

The velocity at the boundary is left to be free. The boundary viscous flux is then calculated as

$$\tilde{\mathcal{H}}_v^I = \tilde{\mathcal{H}}_v^I(\hat{\mathbf{q}}_{BC}, (\nabla \hat{\mathbf{q}})_{in}) \quad (43)$$

Eq. (42) is used as boundary condition for the auxiliary variables in the LDG method, where the derivatives of  $u, v, w, T$  are calculated, and are successively used to evaluate the boundary viscous flux. It is important to note that the boundary viscous flux is computed using the gradients of the inner state since they are unknown at the boundary.

## 2. Numerical results

We tested the outflow BCs in the model problem shown in Fig. 6. Specifically we took into account 6 different combinations as described in Table 5, where *R* stands for reflective pressure outflow BC, *PNR* stands for partially non-reflective pressure outflow BC and *RI* stands for Riemann invariant BC.

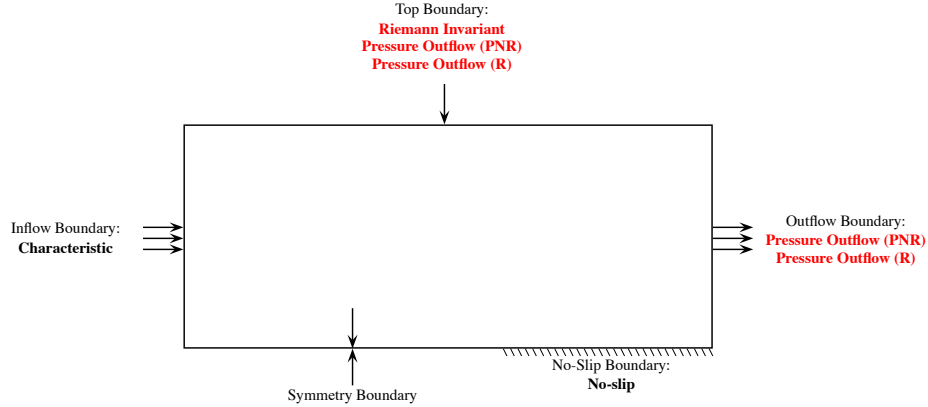
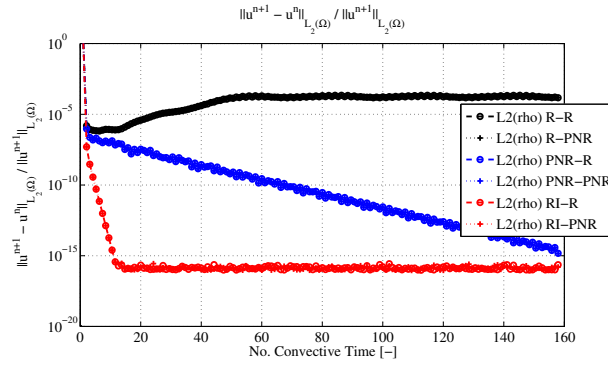


Figure 6. Model problem for *PNR* and *R* pressure outflow BCs

Table 5. Test cases for *PNR* and *R* pressure outflow BCs

Boundary	#1	#2	#3	#4	#5	#6
Top	R	PNR	PNR	R	RI	RI
Outflow	R	PNR	R	PNR	R	PNR



**Figure 7. Convergence to steady state for the 6 different configurations**

We investigated the reflection properties of both the pressure outflow BCs by applying them at the top boundary since multiple reflections of a pressure wave might occur. In particular we compared the reflection properties of the *PNR* and *R* BCs against the Riemann invariant BCs (equivalently the  $\infty$ -value approach in conjunction with an exact Riemann solver). In the case of Riemann invariant BCs the convergence to steady state was achieved after  $\approx 12$  convective times,<sup>c</sup> whereas using the two versions of pressure outflow conditions presented above (i.e. reflective and partially reflective) gave a poor steady-state convergence and in the case of reflective pressure outflow BCs the steady state was wrong, due to an undamped spurious mode trapped within the computational domain. The imposition of a partially non-reflective outflow BCs alleviated this effect by slowly and progressively damping the spurious mode. These features are evident looking at Fig. 8, where for Riemann invariant BCs applied at the top boundary the steady-state error is driven by the geometry (Fig. 8(c)) and its absolute value in terms of the energy field,  $E$ , is of order  $10^{-8}$  Pa, whereas for *R* and *PNR* BCs applied at the top boundary the steady-state error is driven by a spurious mode which is eventually damped in case of *PNR* BC at the top boundary (Fig. 8(b)) while remains undamped in case of *R* BC applied at the top boundary (Fig. 8(a)). In addition, Fig. 8(c) and Fig. 8(d), show that the influence of the outflow boundary on the steady-state solution is negligible since a possibly existing reflected wave is damped when reaches the inflow boundary which uses a characteristic BCs.

One of the important features in this section is that using a difference between an exact and an inner pressure provides a less reflective pressure outflow BCs. Although not clear, we suggest that this might be due to the fact that the difference  $(2p_e - p_{in})$  acts as a penalty term which progressively damps spurious pressure reflections.

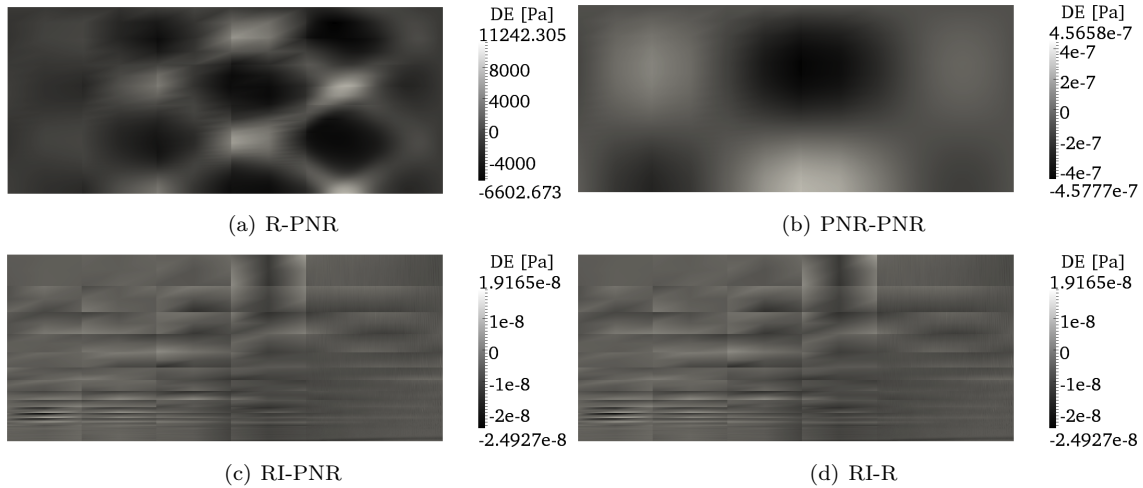


**Figure 8. Difference on the energy field between two consecutive time-steps for 4 different configurations**

<sup>c</sup>The convective time is calculated as the time required by the flow to travel from the inflow to the outflow of the domain:  $t_C = \frac{L}{V_\infty}$  where  $L$  is the length of the computational domain and  $V_\infty$  is the velocity of the flow.

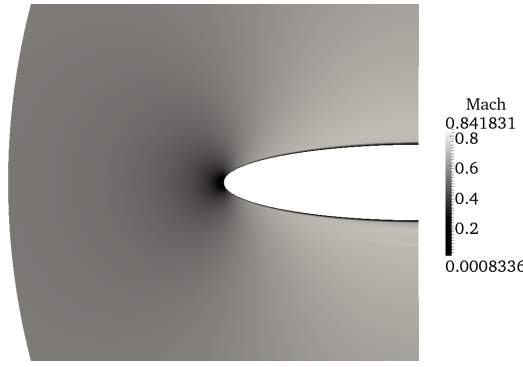


Figure 9. DNS simulation of the leading edge of an aerofoil

In Fig. 9 it is possible to notice how the boundary layer over the leading edge of an aerofoil is left free to develop by applying either a partially non-reflective or a reflective pressure outflow BCs.

We remark here that the purpose of this Section was to give a brief overview on how to implement an outflow boundary condition which takes into account steady viscous effects and not to provide an overall picture on how to implement effective non-reflective boundary conditions for the Navier-Stokes equations since no conclusive work has been produced in the literature.

## B. Non-slip Isothermal and Adiabatic Wall BCs

### 1. Overview - Isothermal

For the Navier-Stokes equations a non-slip condition must be applied to the velocity field at a solid wall. We first consider the treatment of the advection term and successively we describe the diffusion term.

#### Advection term

As previously mentioned, for the advection term we make a distinction on how the BCs are applied. The first is a Weak-Riemann approach and the second is a Weak-Prescribed approach.

- *Weak-Riemann*: We use two different ways for applying a no-slip conditions on the advection term implicitly

*A1*: The first choice is to evaluate the interior velocity field at the boundary  $\mathbf{V}_{in} = [u_{in}, v_{in}, w_{in}]^T$  and then calculate  $\mathbf{V}_- = [u_-, v_-, w_-]$  such that:

$$\mathbf{V}_- = -\mathbf{V}_{in} = -\mathbf{V}_+ \quad (44)$$

Equivalently to the slip BCs, this is done because the condition is imposed implicitly through a Riemann solver which considered the appropriate upwind information from a left (ghost) and right (inner) states.

The density and internal energy are extrapolated from the interior such that the complete ghost state for the advection term of the compressible Navier-Stokes equations in the case of no-slip isothermal BCs is:

$$\mathbf{q}_- = \begin{Bmatrix} \rho_- \\ (\rho u)_- \\ (\rho v)_- \\ (\rho w)_- \\ E_- \end{Bmatrix} = \begin{Bmatrix} \rho_{in} \\ -\rho_{in} u_{in} \\ -\rho_{in} v_{in} \\ -\rho_{in} w_{in} \\ E_{in} \end{Bmatrix} \quad (45)$$

and the boundary flux is calculated through a Riemann solver as follows

$$\tilde{\mathcal{H}}_i^I = \tilde{\mathcal{H}}_i^I(\hat{\mathbf{q}}_+, \hat{\mathbf{q}}_-), \quad (46)$$

where  $\hat{\mathbf{q}}_+$  and  $\hat{\mathbf{q}}_-$  are the inner and the ghost state respectively.

We can see that the only non-zero contribution to the advective flux evaluated by the Riemann solver are those due to the pressure. This is also what we expect by the physical condition of non-slip.

A2: The second choice considered is to set the ghost velocity to zero such that the complete ghost state is

$$\mathbf{q}_- = \begin{Bmatrix} \rho_- \\ (\rho u)_- \\ (\rho v)_- \\ (\rho w)_- \\ E_- \end{Bmatrix} = \begin{Bmatrix} \rho_{in} \\ 0 \\ 0 \\ 0 \\ \frac{p_{in}}{\gamma-1} \end{Bmatrix} \quad (47)$$

and the boundary flux is calculated through a Riemann solver as in Eq. (46).

Also in this case (as for the slip BCs) the Riemann solver incorrectly calculates an intermediate state where the normal component of the velocity is non-zero.

The appropriate choice of the ghost state is constrained by the nature of the Riemann problem at the wall boundary. The choice A1 provides a velocity of the contact wave equal to zero, whereas the choice A2 gives a non-zero velocity for the contact wave. This feature has a profound impact on the accuracy of the no-slip BCs especially for under-resolved meshes. In particular, a non-zero contact wave velocity allows the tangential components of the velocity to be non-zero which in turn affect the pressure and therefore the momentum fluxes as well as, marginally, the mass and energy fluxes. By contrast, the choice A1 provides at each time-step a velocity of the contact wave which is identically zero and therefore the role of the tangential components of the velocity remains negligible.

- *Weak-Prescribed*: The no-slip BCs are imposed explicitly by computing the boundary flux directly from the known solution

$$\mathbf{q}_{BC} = \begin{Bmatrix} \rho_{BC} \\ (\rho u)_{BC} \\ (\rho v)_{BC} \\ (\rho w)_{BC} \\ E_{BC} \end{Bmatrix} = \begin{Bmatrix} \rho_{in} \\ 0 \\ 0 \\ 0 \\ \frac{\rho_{in} R T_w}{\gamma-1} \end{Bmatrix}. \quad (48)$$

where the boundary flux becomes

$$\tilde{\mathcal{H}}_i^I = \tilde{\mathcal{H}}_i^I(\hat{\mathbf{q}}_{BC}) \quad (49)$$

## Diffusion term

For the diffusion term of the compressible Navier-Stokes equations, the auxiliary variables  $\mathbf{q}_{aux}$ , which are used to calculate the first order derivatives, need to be imposed at the boundary. In the case of LDG method in conjunction with an *isothermal wall* with an imposed temperature  $T_w$ , the auxiliary variables at the boundary assume the following values:

$$\mathbf{q}_{aux_{BC}} = \begin{Bmatrix} u_{BC} \\ v_{BC} \\ w_{BC} \\ T_{BC} \end{Bmatrix} = \begin{Bmatrix} 0 \\ 0 \\ 0 \\ T_w \end{Bmatrix}. \quad (50)$$

It is possible to appreciate that the velocity at the boundary is set to zero. The final boundary viscous flux is then calculated as

$$\tilde{\mathcal{H}}_v^I = \tilde{\mathcal{H}}_v^I(\hat{\mathbf{q}}_{BC}, (\nabla \hat{\mathbf{q}})_{in}) \quad (51)$$

Eq. (50) is used as boundary condition for the auxiliary variables in the LDG method, where the derivatives of  $u, v, w, T$  are calculated, and are successively used to evaluate the boundary viscous flux. Also in this case the boundary viscous flux is computed using the gradients of the inner state since they are unknown at the boundary. An exception is the shear stress part of the boundary viscous flux associated to the energy equation which is set to zero, since it is pre-multiplied by the velocity which is known to be zero at a no-slip wall.

## 2. Overview - Adiabatic

The adiabatic no-slip BCs are equivalent to the isothermal no-slip BCs with the only exception that we prescribe the thermal flux instead of the temperature at the wall.

### Advection term

The advection term in this case is exactly equivalent to the isothermal no-slip wall BCs, with the same two Weak-Riemann cases A1, Eq. (45) and A2, Eq. (47) as well as with the same Weak-Prescribed state Eq. (48).

### Diffusion term

The diffusion term for an *adiabatic wall* differs from the isothermal since we apply the thermal flux instead of the wall temperature. Specifically the temperature at the boundary is extrapolated from the interior and the dependent variables at the wall are

$$\mathbf{q}_{auxBC} = \begin{Bmatrix} u_{BC} \\ v_{BC} \\ w_{BC} \\ T_{BC} \end{Bmatrix} = \begin{Bmatrix} 0 \\ 0 \\ 0 \\ T_{in} \end{Bmatrix}. \quad (52)$$

Eq. (52) is used as the boundary condition for the auxiliary system in the LDG method.

In order to evaluate the normal flux at the boundary, we need to split the flux in Eq. (11) into two parts: one which arises from the shear stresses (superscript  $s$  in Eq. (53)), and one which depends on the thermal diffusivity (superscript  $t$  in Eq. (53)):

$$\begin{aligned} \mathbf{F}^s &= \begin{Bmatrix} 0 \\ \tau_{xx} \\ \tau_{yx} \\ \tau_{zx} \\ u\tau_{xx} + v\tau_{yx} + w\tau_{zx} \end{Bmatrix}, & \mathbf{F}^t &= \begin{Bmatrix} 0 \\ 0 \\ 0 \\ 0 \\ kT_x \end{Bmatrix}, \\ \mathbf{G}^s &= \begin{Bmatrix} 0 \\ \tau_{xy} \\ \tau_{yy} \\ \tau_{zy} \\ u\tau_{xy} + v\tau_{yy} + w\tau_{zy} \end{Bmatrix}, & \mathbf{G}^t &= \begin{Bmatrix} 0 \\ 0 \\ 0 \\ 0 \\ kT_y \end{Bmatrix}, \\ \mathbf{H}^v &= \begin{Bmatrix} 0 \\ \tau_{xz} \\ \tau_{yz} \\ \tau_{zz} \\ u\tau_{xz} + v\tau_{yz} + w\tau_{zz} \end{Bmatrix}, & \mathbf{H}^t &= \begin{Bmatrix} 0 \\ 0 \\ 0 \\ 0 \\ kT_z \end{Bmatrix}, \end{aligned} \quad (53)$$

At the boundary, the normal flux arising from the shear stresses is extrapolated from the values obtained in the interior of the domain while the normal flux arising from the thermal diffusivity is set to zero, i.e.

$$k\nabla T \cdot \mathbf{n} = 0. \quad (54)$$

## 3. Numerical results

We present the results for the isothermal BCs only since the conclusions drawn for the adiabatic BCs are identical.

The isothermal no-slip BCs have been evaluated using the model problem in Fig. 10. Specifically we used a flat-plate mesh composed of 2592 quadrilaterals and divided into 5 different boundary regions: *Inflow*, *Symmetry*, *No-slip wall*, *Outflow* and *Farfield*.

The flat-plate started at  $x = 0[m]$  and ended at  $x = 0.02[m]$ . The inflow was located at  $x = -0.05[m]$  and the height of the mesh was  $h = 0.03[m]$ . As boundary condition configuration we used a characteristic treatment of the *Inflow* and *Farfield* regions, a pressure outflow partially non-reflective (PNR) BCs for the *Outflow*, a symmetry (slip) BCs prior to the flat-plate and a no-slip isothermal BCs at the *Wall*.

All the results presented in this Section were obtained for a subsonic Mach number  $M_\infty = 0.5$  and a Reynolds number equal to  $Re_{L=1} = 10^6$ . Additional tests were performed at a supersonic Mach number equal to  $M_\infty = 1.5$ , which provided similar results if compared to the subsonic case in terms of no-slip BCs. In particular it was observed a rather important aliasing issue for the *Weak-Riemann-A2* and for the *Weak-Prescribed* approaches whilst the *Weak-Riemann-A1* was more robust throughout the tests performed, showing moderate aliasing problems.

For all the simulations performed we employed a two-stage Runge-Kutta as time-integration scheme and we used the FR scheme for the inviscid flux and the LDG approach for the viscous flux.

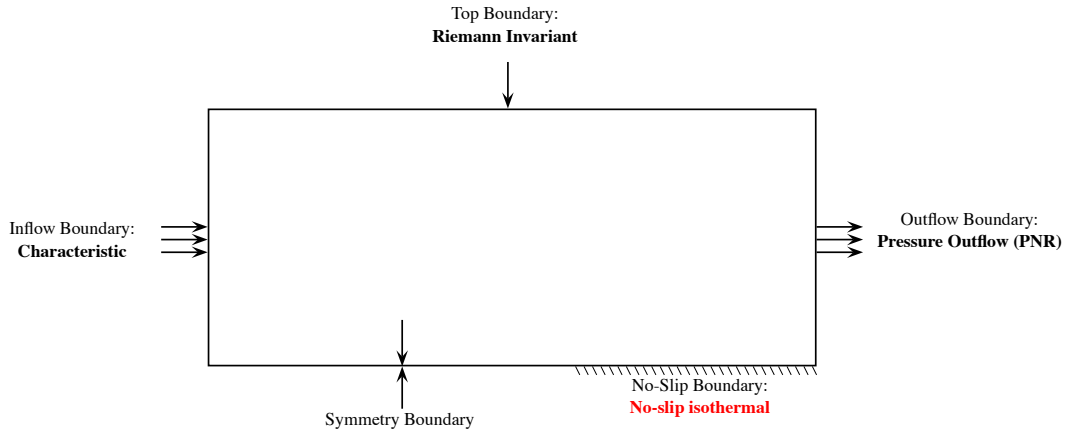


**Figure 10. Model problem for no-slip isothermal BCs**

We took into account three different polynomial orders,  $\mathcal{P} = 2, 4, 6$  and a Weak-Prescribed (Eq. (48)) as well as two different Weak-Riemann approaches for applying the BCs: *Weak-Riemann-A1* (Eq. (45)) and *Weak-Riemann-A2* (Eq. (47)). In addition we used an exact Riemann solver as well as two approximated Riemann solvers: HLL and HLLC.

The evaluation of the no-slip isothermal BCs has been carried out by investigating the convergence to steady-state and by comparing four dimensional quantities at the wall:  $u$  - horizontal component of the velocity,  $v$  - vertical component of the velocity,  $L$  - lift and  $D$  - drag. For all the simulations, we used a time-step such that the error due to the time-stepping was negligible.

In Fig. 11 we show the behaviour of the velocities  $u$  and  $v$  at the wall along the flat-plate by varying the polynomial order. The flat-plate can be divided into two regions, the leading edge region which is affected by strong gradients of the variables and a region sufficiently far from the leading edge which we arbitrarily decided to be comprised in the range  $x \in [0.015m; 0.02m]$ . For  $\mathcal{P} = 2$  the solution took more space to recover a flat solution 'equal' to zero for both the velocities  $u$  and  $v$ . By increasing the polynomial order the flat solution was recovered much prior as expected (since the boundary layer was better resolved).

Fig. 12 shows the same quantities as Fig. 11 by varying the BC approach. Remarkable is the poor performance obtained by the Weak-Riemann-A2 approach. Small difference can also be noticed between the Weak-Prescribed and the Weak-Riemann-A1 approaches especially on the normal velocity  $v$  (Fig. 12(b)) which, for Weak-Prescribed approach, presents a large oscillation in proximity to the leading edge.

In Fig. 13 we show the same variables as in the previous two described figures by varying the Riemann solver employed. No differences can be noticed.

The observations made for Figures 11, 12 and 13 are quantified in the Tables. In Table 6 we show the averages of the tangential ( $u_b$ ) and normal ( $v_b$ ) velocities at the wall in the domain  $x \in [0.015m; 0.02m]$ , as functions of the polynomial order  $\mathcal{P}$  as well as of the BC approach. In this region, aliasing effects at the wall

are minimal since we are sufficiently far from the leading edge where the aliasing issues are quite significant.

The Weak-Prescribed and the Weak-Riemann-A1 approaches perform similarly for the smallest polynomial order  $\mathcal{P} = 2$  on both the tangential and the normal velocity. On the other hand the Weak-Riemann-A2 approach provides very poor results as shown in Fig. 14(a) where we plotted the compressible similarity solution for the velocity  $u$  at  $X = 0.015m$  for  $\mathcal{P} = 2$ . For  $\mathcal{P} = 4$  and  $\mathcal{P} = 6$  the Weak-Prescribed approach is affected by aliasing and the simulations diverged without using a de-aliasing technique (i.e. using an exact quadrature to integrate the nonlinear terms) whereas the two Weak-Riemann approaches did not give any problem on this regard. Particularly interesting is to notice how the Weak-Riemann-A2 produces both tangential and normal velocity components that are twice the value for the Weak-Riemann-A1 approach. This is consistent with the Riemann problem being solved at the wall interface. Also, the Weak-Riemann-A2 approach recovered a correct behaviour of the velocity profile if compared against the similarity solution as shown in Fig. 14(b).

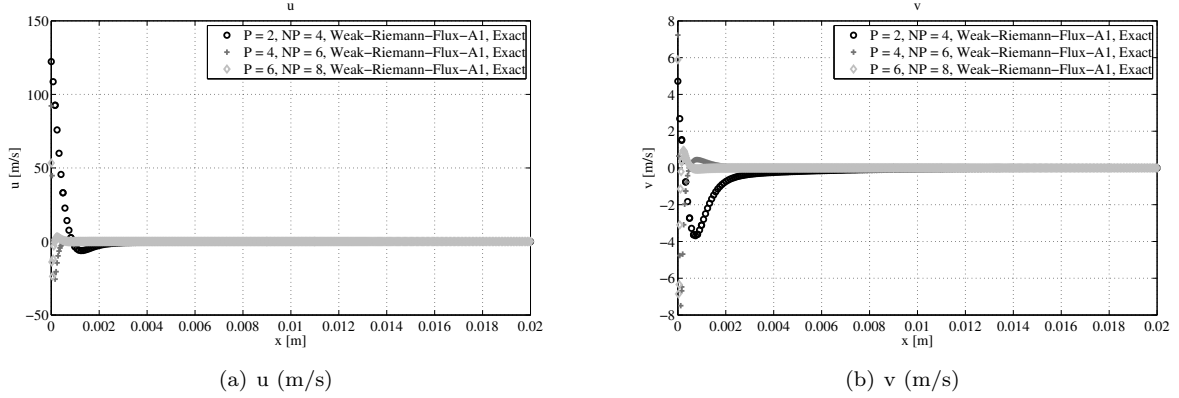


Figure 11. Comparison of wall velocities  $u$  [11(a)] and  $v$  [11(b)] between 3 different polynomial orders,  $\mathcal{P}=2$  (black circles),  $\mathcal{P}=4$  (grey pluses) and  $\mathcal{P}=6$  (light grey diamonds) for Weak-Riemann-A1 BCs; no-slip isothermal BCs

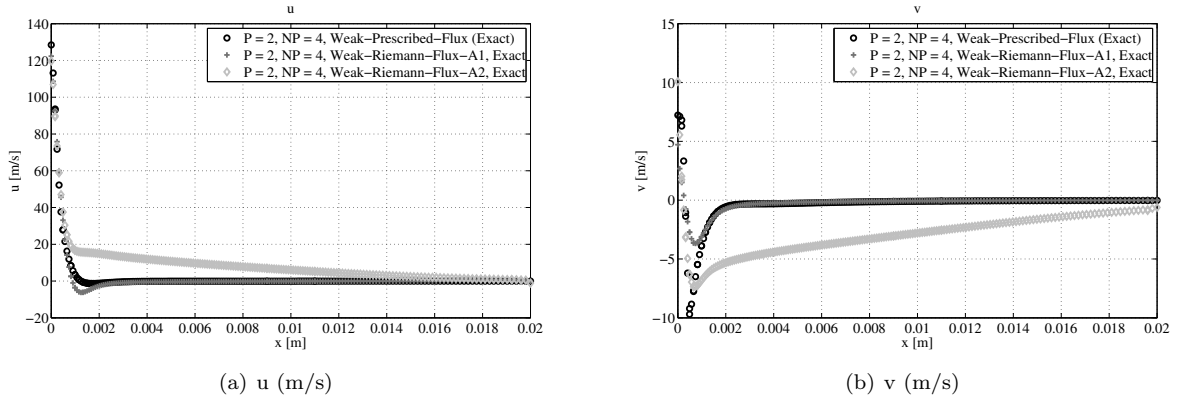
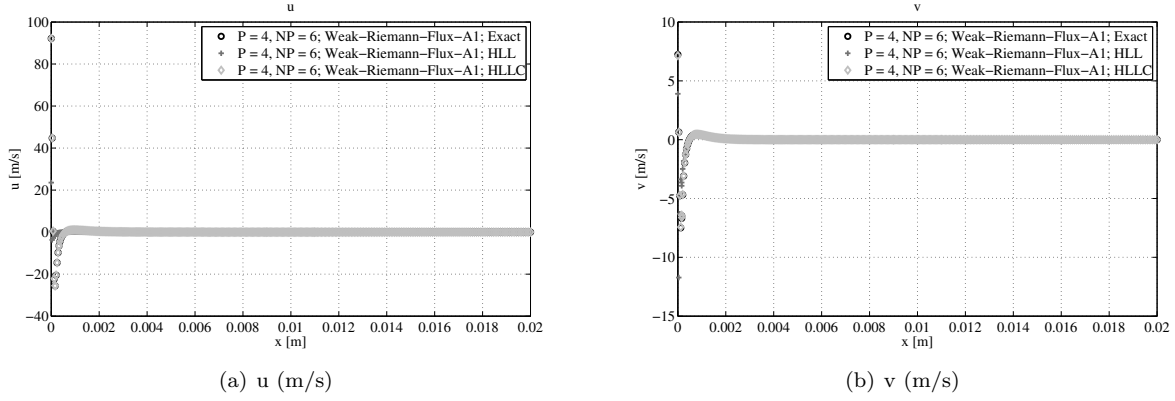


Figure 12. Comparison of wall velocities  $u$  [12(a)] and  $v$  [12(b)] between Weak-Prescribed BCs (black circles), Weak-Riemann-A1 BCs (grey pluses) and Weak-Riemann-A1 BCs (light grey diamonds) for  $\mathcal{P}=2$ ; no-slip isothermal BCs



**Figure 13.** Comparison of wall velocities  $u$  [13(a)] and  $v$  [13(b)] between Exact Riemann solver (black circles), HLL (grey pluses) and HLLC BCs (light grey diamonds) for  $P=4$  and Weak-Riemann-A1 approach; no-slip isothermal BCs

**Table 6.** Velocity  $u_b$  ( $x$ -component) and  $v_b$  ( $y$ -component) at the wall as functions of the polynomial order and of the BC approach for exact Riemann solver. The values of  $u_b$  and  $v_b$  are averages of the velocities at the solution points in the domain comprised between  $x \in [0.015m; 0.02m]$

	$ \mathbf{u}_b [\text{m/s}]$		
	$\mathcal{P} = 2$	$\mathcal{P} = 4$	$\mathcal{P} = 6$
<b>Weak-Riemann-A1</b>	$-5.1247 \times 10^{-2}$	$6.0049 \times 10^{-4}$	$6.9850 \times 10^{-6}$
<b>Weak-Riemann-A2</b>	$1.4755 \times 10^0$	$6.2401 \times 10^{-4}$	$7.1231 \times 10^{-6}$
<b>Weak-Prescribed</b>	$2.9327 \times 10^{-2}$	aliasing ( $7.5101 \times 10^{-4}$ )	aliasing ( $6.3312 \times 10^{-6}$ )
	$ \mathbf{v}_b [\text{m/s}]$		
	$\mathcal{P} = 2$	$\mathcal{P} = 4$	$\mathcal{P} = 6$
<b>Weak-Riemann-A1</b>	$1.8109 \times 10^{-2}$	$3.5626 \times 10^{-4}$	$1.2274 \times 10^{-6}$
<b>Weak-Riemann-A2</b>	$1.1821 \times 10^0$	$7.1523 \times 10^{-4}$	$2.4188 \times 10^{-6}$
<b>Weak-Prescribed</b>	$3.0906 \times 10^{-2}$	aliasing ( $-5.8827 \times 10^{-4}$ )	aliasing ( $2.0545 \times 10^{-6}$ )

In Table 7 we show the error on lift and drag again as function of the polynomial order as well as of the BC approach used. In this case the two indicators include the entire flat-plate (including the leading edge) therefore the aliasing issues due the coarseness of the mesh come into the picture. It can still be appreciated that the Weak-Riemann-A1 approach provides the most robust results consistently with what seen in Table 6.

Tables 8 and 9 present the same results, wall velocities, lift and drag as functions of the Riemann solver used and of the BC approach.

Interestingly the HLL solver performed better than the HLLC and the exact solvers for what concerned the tangential velocity. For all the Riemann solvers tested the Weak-Riemann-A1 approach revealed to have superior performance with respect to the others (except for the lift in case of HLL Riemann solver).



Table 7. Lift  $L$  as a function of the polynomial order and of the flux technique used at the boundary (Exact Riemann solver): no-slip isothermal BCs

	$ \mathbf{L} - \mathbf{L}_{exact} [\text{N}]$		
	$\mathcal{P} = 2$	$\mathcal{P} = 4$	$\mathcal{P} = 6$
<b>Weak-Riemann-A1</b>	0.4680	0.0260	0.0080
<b>Weak-Riemann-A2</b>	3.37	0.04	0.03
<b>Weak-Prescribed</b>	0.0520	aliasing (0.0540)	aliasing (0.0320)
	$ \mathbf{D} - \mathbf{D}_{exact} [\text{N}]$		
	$\mathcal{P} = 2$	$\mathcal{P} = 4$	$\mathcal{P} = 6$
<b>Weak-Riemann-A1</b>	0.09	0.0050	0.0067
<b>Weak-Riemann-A2</b>	0.5819	0.0834	0.0215
<b>Weak-Prescribed</b>	0.1126	aliasing (0.0126)	aliasing (0.0042)

Table 8. Velocity  $u_b$  ( $x$ -component ) at the wall as a function of the Riemann solver employed and of the flux technique used at the boundary for  $P = 4$ : no-slip isothermal BCs

	$ \mathbf{u}_b [\text{m/s}]$		
	Exact	HLL	HLLC
<b>Weak-Riemann-A1</b>	$6.0049 \times 10^{-4}$	$-8.8157 \times 10^{-6}$	$6.0048 \times 10^{-4}$
<b>Weak-Riemann-A2</b>	$6.2401 \times 10^{-4}$	$-1.8435 \times 10^{-5}$	$6.2372 \times 10^{-4}$
<b>Weak-Prescribed</b>	aliasing ( $7.5101 \times 10^{-4}$ )	aliasing ( $-7.1791 \times 10^{-5}$ )	aliasing ( $7.5099 \times 10^{-5}$ )
	$ \mathbf{v}_b [\text{m/s}]$		
	Exact	HLL	HLLC
<b>Weak-Riemann-A1</b>	$-3.5626 \times 10^{-4}$	$-4.0725 \times 10^{-4}$	$-3.5625 \times 10^{-4}$
<b>Weak-Riemann-A2</b>	$-7.1523 \times 10^{-4}$	$-8.2296 \times 10^{-4}$	$-7.1503 \times 10^{-4}$
<b>Weak-Prescribed</b>	aliasing ( $-5.8827 \times 10^{-4}$ )	aliasing ( $-6.8178 \times 10^{-4}$ )	aliasing ( $-5.8826 \times 10^{-4}$ )

Table 9. Lift  $L$  as a function of the Riemann solver employed and of the flux technique used at the boundary for  $P = 4$ : no-slip isothermal BCs

	$ \mathbf{L} - \mathbf{L}_{exact} [\text{N}]$		
	Exact	HLL	HLLC
<b>Weak-Riemann-A1</b>	0.026	0.098	0.026
<b>Weak-Riemann-A2</b>	0.04	0.02	0.04
<b>Weak-Prescribed</b>	aliasing (0.054)	aliasing (0.054)	aliasing ( 0.054)
	$ \mathbf{D} - \mathbf{D}_{exact} [\text{N}]$		
	Exact	HLL	HLLC
<b>Weak-Riemann-A1</b>	0.005	0.0021	0.0049
<b>Weak-Riemann-A2</b>	0.0834	0.0842	0.0825
<b>Weak-Prescribed</b>	aliasing (0.0126)	aliasing (0.0123)	aliasing (0.0126)

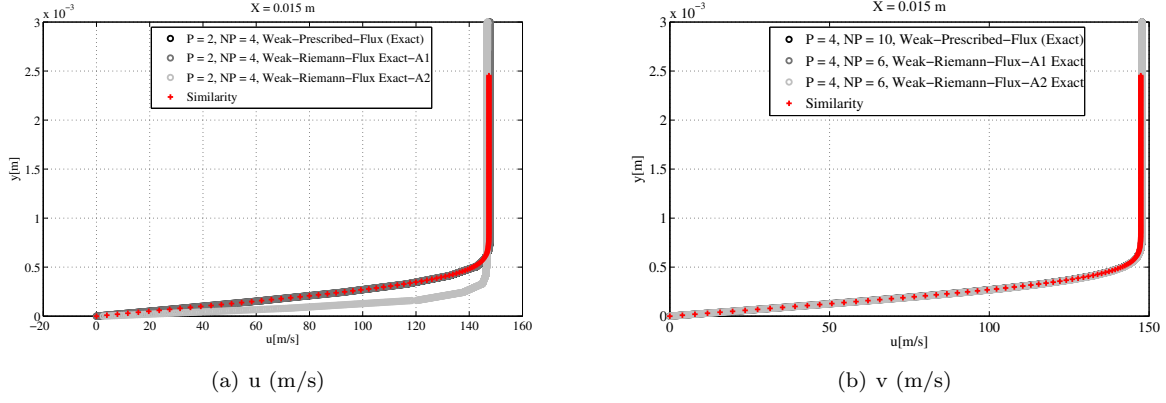


Figure 14. Similarity solution vs. numerical solution for  $u$  and  $P=2$  [14(a)] as well as  $P=4$  [14(b)]. Weak-Prescribed BCs (black dashed line), Weak-Riemann-A1 BCs (grey dashed line), Weak-Riemann-A2 BCs (light grey dashed line) and similarity solution (red dashed line); no-slip isothermal BCs

Finally, considering the convergence to steady-state, in Fig. 15 we show the convergence history of  $\rho u$  at the wall (Fig. 15(a)) and the convergence history of the same variable for the entire domain (Fig. 15(b)). The convergence history on the entire domain is driven by the wall convergence history but no significant differences can be seen between the various BC approaches used.

On the other hand, in Fig. 16, where we show the convergence history of the  $\rho v$  variable for the wall (Fig. 16(a)) and for the entire domain (16(b)), a quite larger difference can be noticed between the Weak-Riemann-A1 approach and the Weak-Riemann-A2 approach. In particular the second performs worse than the first providing a slightly slower convergence<sup>d</sup>.

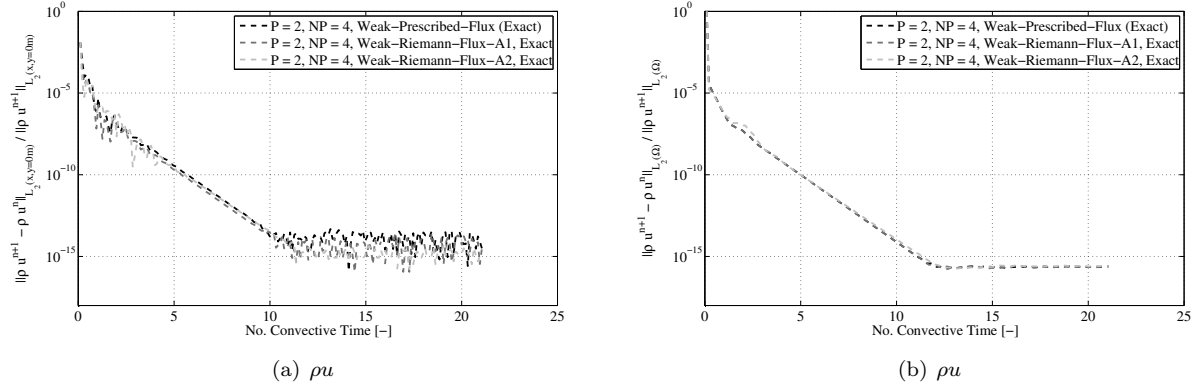
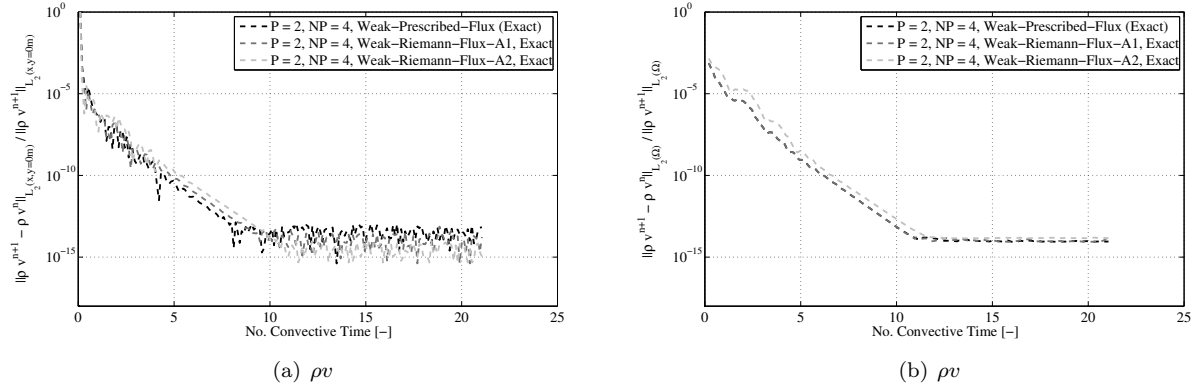


Figure 15. Convergence history of the  $\rho u$  residual at the wall [15(a)] and convergence history of the  $\rho u$  residual on the entire computational domain [15(b)] for Weak-Prescribed BCs (black dashed line), Weak-Riemann-A1 BCs (grey dashed line) and Weak-Riemann-A2 BCs (light grey dashed line); no-slip isothermal BCs

<sup>d</sup>The convective time is calculated as specified in the slip BCs Section



**Figure 16.** Local convergence history of the  $\rho v$  residual at the wall [16(a)] and global convergence history of the  $\rho v$  residual [16(b)] for Weak-Prescribed BCs (black dashed line), Weak-Riemann-A1 BCs (grey dashed line) and Weak-Riemann-A2 BCs (light grey dashed line); no-slip isothermal BCs

To conclude this Section we observe that consistent results were obtained between slip and no-slip conditions and a Weak-Riemann-A1 strategy revealed to be the most effective (at least for under-resolved problems) and robust. This result is consistent with what reported by Nordstorm et al.<sup>1,7,8</sup>

In addition, the Weak-Prescribed strategy was affected by aliasing issues which can be alleviated by de-aliasing the nonlinear terms of the equations (in particular by using an exact integration of the nonlinear terms).

## V. Conclusions

In this paper different types of weak boundary conditions for the Euler and the compressible Navier-Stokes equations were systematically described and tested in the context of discontinuous compact high-order methods. We have found that the use of exact or approximated Riemann solvers (Weak-Riemann approach) is effective and the most robust for applying the boundary conditions if associated with the correct ghost state. We have also found that the application of boundary conditions by calculating the flux with the known solution at the boundary (Weak-Prescribed approach) is affected by aliasing issues (for slip and no-slip BCs) which can be alleviated by using an exact quadrature for integrating the nonlinear terms.

We considered inflow/outflow and wall boundary conditions both slip (for the Euler equations) and no-slip (isothermal and adiabatic for the compressible Navier-Stokes equations).

For the Euler equations we described the implementation of Riemann invariant (characteristic) boundary conditions and we showed how an  $\infty$ -value approach (i.e. applying the  $\infty$  state as ghost state) in conjunction with exact or approximated Riemann solvers in a Weak-Riemann approach is equivalent to calculating the Riemann invariants associated to the problem and applying them as boundary conditions in a Weak-Prescribed sense. In addition we showed how the use of a simple average solver produced a much greater reflection than all the other cases. Finally we showed how the application of the  $\infty$  state applied in Weak-Prescribed sense led to an unstable simulation.

Considering the slip conditions for the Euler equations we showed how different types of implementation strategies affect the solution in terms of normal velocity at the wall, lift, drag as well as in terms of robustness. It was found that the most robust implementation was achieved by applying a Weak-Riemann approach and using as ghost state the configuration A1. The Weak-Prescribed and Weak-Riemann-A2 approaches were both affected by aliasing issues which led the simulations to diverge. Interestingly the application of the BCs in a Weak-Riemann-A1 way was also the most accurate in terms of normal velocity at the wall.

In the case of Navier-Stokes equations we explored the Farfield / outflow conditions by considering as model problem the flat-plate test case. In this case we described two different types of pressure outflow boundary conditions,  $PNR$  and  $R$ , which can be applied at a given outflow in presence of steady (laminar) viscous effects. We showed how  $PNR$  was less reflective than  $R$  by applying these pressure outflow boundary conditions at the top wall of the model problem. We also compared their performance in terms of reflection against the Riemann invariant boundary conditions, showing how such pressure outflow boundary conditions,

either  $PNR$  or  $R$  does not recover the same reflection properties of the characteristic boundary conditions. The interesting point of this Section was that  $R$  produced a spurious undamped acoustic mode which remained trapped within the computational domain leading the simulation to converge to an erroneous steady state solution whereas the  $PNR$  recovered, despite slowly, the correct steady state solution because the spurious acoustic mode was progressively damped in time.

Finally, for what concerns the no-slip boundary conditions for the Navier-Stokes equations we described both the isothermal and the adiabatic cases. Also for the no-slip BCs as for the slip BCs, the Weak-Riemann-A1 approach was the most robust whereas Weak-Riemann-A2 and Weak-Prescribed were affected by aliasing. In particular, for the smallest polynomial order Weak-Riemann-A2 provided a very poor result whereas Weak-Riemann-A1 and Weak-Prescribed performed better providing moderate values of slip velocity.

The Weak-Riemann-A1 approach revealed to be the most robust in terms of aliasing issues for both slip and no-slip conditions. The Weak-Prescribed approach provided results comparable to Weak-Riemann-A1 where it was not affected by aliasing issues. The Weak-Riemann-A2 approach was quite sensitive to the coarseness of the mesh employed (small polynomial order) providing poor results. However, for higher polynomial orders it eventually recovered similar results to the Weak-Riemann-A1 and Weak-Prescribed approaches.

## Acknowledgments

This work was supported by the Laminar Flow Control Centre funded by Airbus/EADS and EPSRC under grant EP/I037946. GM wants to acknowledge Dr. Shahid Mughal for providing the similarity solutions as well as Dr. Hui Xu and Dr. David Moxey for some fruitful discussions.

## Appendix

### A. Riemann solvers

The role of the Riemann solvers in the context of compact high-order methods is crucial. They allow the various elements of the numerical discretisations to communicate and are also responsible for the boundary conditions to be correctly transferred into the domain in the case of BCs treatment through a Weak-Riemann approach.

In the following we describe some relevant Riemann solvers employed by using a similar nomenclature as in the book by Toro.<sup>20</sup> In particular we consider the 3D Euler equation and its associated Riemann problem (Fig. 17) which is composed by two nonlinear waves (dotted lines) associated with the maximum and minimum eigenvalue of the system (shock waves or rarefaction waves), and by three contact waves (dashed line) associated with the three coincident eigenvalues of the problem.

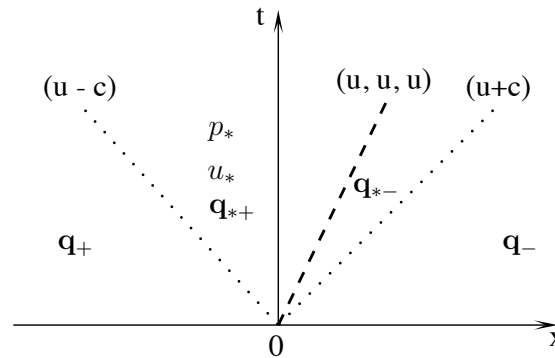


Figure 17. Riemann problem for the Euler equations with ideal gas law

The region between the two nonlinear waves is denoted as the star region in the following and the left and right states are denoted with the subscripts  $+$  and  $-$  respectively. The nature of the solution strictly depends on the equation of state. In all the cases considered in this work we use an ideal gas law.

We also remark that the use of a Riemann solver at the interface between two elements can be cast more

in general in the numerical setting of Godunov-type methods such as the finite volume schemes for which a large amount of work has been carried out in the past decades.

When using a Riemann solver at a given interface it is necessary to rotate the 2D/3D problem into a 1D problem in the normal direction with respect to the given interface. By exploiting the rotational invariance of the Euler equations it is possible to write

$$[\mathbf{f}_i \quad \mathbf{g}_i \quad \mathbf{h}_i] \begin{bmatrix} \cos(\theta_y) \cos(\theta_z) \\ \cos(\theta_y) \sin(\theta_z) \\ \sin(\theta_y) \end{bmatrix} = \mathbf{R}^{-1} \mathbf{f}(\mathbf{R}\mathbf{q}), \quad (55)$$

where  $\theta_y, \theta_z$  are the angles which link a normal frame of reference to the Cartesian frame of reference,  $\mathbf{R}$  is the following rotation matrix

$$\begin{bmatrix} 1 & 0 & 0 & 0 & 0 \\ 0 & \cos(\theta_y) \cos(\theta_z) & \cos(\theta_y) \sin(\theta_z) & \sin(\theta_y) & 0 \\ 0 & -\sin(\theta_z) & \cos(\theta_z) & 0 & 0 \\ 0 & -\sin(\theta_y) \cos(\theta_z) & -\sin(\theta_y) \sin(\theta_z) & \cos(\theta_y) & 0 \\ 0 & 0 & 0 & 0 & 1 \end{bmatrix}. \quad (56)$$

and  $\mathbf{R}^{-1}$  is its inverse. From a practical implementative point of view it is common to first apply the rotation matrix  $\mathbf{R}$  to the variables  $\mathbf{q}$  in order to calculate the augmented one-dimensional flux

$$\mathbf{f}(\mathbf{q}_n) = \mathbf{f}(\mathbf{R}\mathbf{q}). \quad (57)$$

Successively one rotates the augmented one-dimensional flux back to the cartesian frame of reference by multiplying by the inverse of the rotation matrix using Eq. (55). It is important to notice here that the final flux obtained is projected into the normal direction of the interface.

The intermediate step between the two rotations is to calculate the augmented one-dimensional flux. At this stage different Riemann solvers can be used depending on the performance (dissipation, dispersion properties, stability, computational costs) one desires to obtain.

In the the following we briefly describe three Riemann solvers which have been widely used throughout our numerical result sections, an exact Riemann solver and two approximated Riemann solvers, HLL and HLLC.

#### Exact :

The Exact Riemann solver uses the exact solution of the Riemann problem for the Euler equations. It is well-known that there are ten possible wave patterns allowed at an interface and if we use a local frame of reference with respect to the interface, this reduces in solving the Riemann problem in the space-time plane for  $x/t = 0$ . The first step to perform is therefore to identify which pattern has arisen at a given interface and successively calculate the boundary state  $\mathbf{q}_n$  (and consequently the augmented one-dimensional flux  $\mathbf{f}(\mathbf{q}_n)$ ) for  $x/t = 0$ .

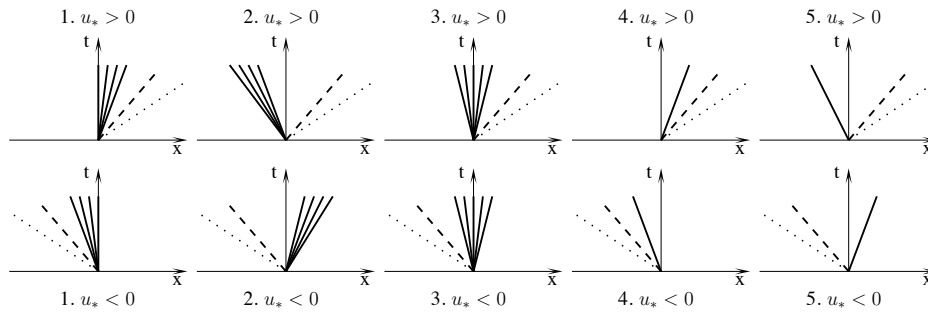


**Figure 18. Possible wave patterns of the exact Riemann solver for the Euler equation**

In particular we have two macro cases each of those in turn divided into five sub-cases:

- Positive particle speed in the region between the two nonlinear waves (star region),  $u_* \geq 0$ 
  1. Left rarefaction -  $\mathbf{q}_+$ : if  $p_* \leq p_+$  and  $u_+ \geq c_+$  we have a left rarefaction wave with a left state which is supersonic and the state for  $x/t = 0$  is the left state. Consequently the boundary fluxes in the normal frame of reference with respect to a given interface are

$$\begin{cases} \mathcal{H}_\rho^{\delta I} = \rho_+ u_+ \\ \mathcal{H}_{\rho u}^{\delta I} = \rho_+ u_+^2 + p_+ \\ \mathcal{H}_{\rho v}^{\delta I} = \rho_+ u_+ v_+ \\ \mathcal{H}_{\rho w}^{\delta I} = \rho_+ u_+ w_+ \\ \mathcal{H}_E^{\delta I} = u_+ \left[ \frac{p_+}{\gamma-1} + \frac{1}{2} \rho_L (u_+^2 + v_+^2 + w_+^2) + p_+ \right] \end{cases} \quad (58)$$

2. Left rarefaction -  $\mathbf{q}_{*+}$ : if  $p_* \leq p_+$ ,  $u_+ < c_+$ , and  $u_* < c_+ \left( \frac{p_*}{p_+} \right)^{\frac{\gamma-1}{2\gamma}}$  we have a left rarefaction wave with a left state which is subsonic and the state for  $x/t = 0$  is the star left state. The boundary fluxes in this case are

$$\begin{cases} \mathcal{H}_\rho^{\delta I} = \rho_+ \left( \frac{p_*}{p_+} \right)^{\frac{1}{\gamma}} u_* \\ \mathcal{H}_{\rho u}^{\delta I} = \rho_+ \left( \frac{p_*}{p_+} \right)^{\frac{1}{\gamma}} u_*^2 + p_* \\ \mathcal{H}_{\rho v}^{\delta I} = \rho_+ \left( \frac{p_*}{p_+} \right)^{\frac{1}{\gamma}} u_* v_+ \\ \mathcal{H}_{\rho w}^{\delta I} = \rho_+ \left( \frac{p_*}{p_+} \right)^{\frac{1}{\gamma}} u_* w_+ \\ \mathcal{H}_E^{\delta I} = u_* \left[ \frac{p_*}{\gamma-1} + \frac{1}{2} \rho_+ \left( \frac{p_*}{p_+} \right)^{\frac{1}{\gamma}} (u_*^2 + v_+^2 + w_+^2) + p_* \right] \end{cases} \quad (59)$$

3. Left rarefaction -  $\mathbf{q}_{+Fan}$ : if  $p_* \leq p_+$ ,  $u_+ < c_+$  and  $u_* \geq c_+ \left( \frac{p_*}{p_+} \right)^{\frac{\gamma-1}{2\gamma}}$  we have a left rarefaction wave with a left state which is subsonic and the state for  $x/t = 0$  is the rarefaction fan. The boundary fluxes in this case are

$$\begin{cases} \mathcal{H}_\rho^{\delta I} = \rho_+ \left[ \frac{2}{\gamma+1} + \frac{\gamma-1}{\gamma+1} \left( \frac{u_+}{c_+} \right) \right]^{\frac{2}{\gamma-1}} \left( \frac{2c_+}{\gamma+1} + \frac{\gamma-1}{\gamma+1} u_+ \right) \\ \mathcal{H}_{\rho u}^{\delta I} = \rho_+ \left[ \frac{2}{\gamma+1} + \frac{\gamma-1}{\gamma+1} \left( \frac{u_+}{c_+} \right) \right]^{\frac{2}{\gamma-1}} \left( \frac{2c_+}{\gamma+1} + \frac{\gamma-1}{\gamma+1} u_+ \right)^2 + p_+ \left[ \frac{2}{\gamma+1} + \frac{\gamma-1}{\gamma+1} \left( \frac{u_+}{c_+} \right) \right]^{\frac{2\gamma}{\gamma-1}} \\ \mathcal{H}_{\rho v}^{\delta I} = \rho_+ \left[ \frac{2}{\gamma+1} + \frac{\gamma-1}{\gamma+1} \left( \frac{u_+}{c_+} \right) \right]^{\frac{2}{\gamma-1}} \left( \frac{2c_+}{\gamma+1} + \frac{\gamma-1}{\gamma+1} u_+ \right) v_+ \\ \mathcal{H}_{\rho w}^{\delta I} = \rho_+ \left[ \frac{2}{\gamma+1} + \frac{\gamma-1}{\gamma+1} \left( \frac{u_+}{c_+} \right) \right]^{\frac{2}{\gamma-1}} \left( \frac{2c_+}{\gamma+1} + \frac{\gamma-1}{\gamma+1} u_+ \right) w_+ \\ \mathcal{H}_E^{\delta I} = \left( \frac{2c_+}{\gamma+1} + \frac{\gamma-1}{\gamma+1} u_+ \right) \left\{ \frac{p_+ \left[ \frac{2}{\gamma+1} + \frac{\gamma-1}{\gamma+1} \left( \frac{u_+}{c_+} \right) \right]^{\frac{2\gamma}{\gamma-1}}}{\gamma-1} + \right. \\ \left. + \frac{1}{2} \rho_+ \left[ \frac{2}{\gamma+1} + \frac{\gamma-1}{\gamma+1} \left( \frac{u_+}{c_+} \right) \right]^{\frac{2}{\gamma-1}} \left[ \left( \frac{2c_+}{\gamma+1} + \frac{\gamma-1}{\gamma+1} u_+ \right)^2 + v_+^2 + w_+^2 \right] + \right. \\ \left. + p_+ \left[ \frac{2}{\gamma+1} + \frac{\gamma-1}{\gamma+1} \left( \frac{u_+}{c_+} \right) \right]^{\frac{2\gamma}{\gamma-1}} \right\} \end{cases} \quad (60)$$

4. Left shock -  $\mathbf{q}_+$ : if  $p_* > p_+$  and  $u_+ \geq c_+ \left( \frac{\gamma+1}{2\gamma} \frac{p_*}{p_+} + \frac{\gamma-1}{2\gamma} \right)^{\frac{1}{2}}$ , we have a left shock with the state for  $x/t = 0$  being the left state. The associated boundary fluxes are

$$\begin{cases} \mathcal{H}_\rho^{\delta I} = \rho_+ u_+ \\ \mathcal{H}_{\rho u}^{\delta I} = \rho_+ u_+^2 + p_+ \\ \mathcal{H}_{\rho v}^{\delta I} = \rho_+ u_+ v_+ \\ \mathcal{H}_{\rho w}^{\delta I} = \rho_+ u_+ w_+ \\ \mathcal{H}_E^{\delta I} = u_+ \left[ \frac{p_+}{\gamma-1} + \frac{1}{2} \rho_L (u_+^2 + v_+^2 + w_+^2) + p_+ \right] \end{cases} \quad (61)$$

5. Left shock -  $\mathbf{q}_{*+}$ : if  $p_* > p_+$  and  $u_+ < c_+ \left( \frac{\gamma+1}{2\gamma} \frac{p_*}{p_+} + \frac{\gamma-1}{2\gamma} \right)^{\frac{1}{2}}$ , we have a left shock with the

state for  $x/t = 0$  being the left star state. The associated boundary fluxes are

$$\left\{ \begin{array}{l} \mathcal{H}_\rho^{\delta I} = \rho_+ \left( \frac{\frac{p_*}{p_+} + \frac{\gamma-1}{\gamma+1}}{\frac{p_*}{p_+} \frac{\gamma-1}{\gamma+1} + 1} \right) u_* \\ \mathcal{H}_{\rho u}^{\delta I} = \rho_+ \left( \frac{\frac{p_*}{p_+} + \frac{\gamma-1}{\gamma+1}}{\frac{p_*}{p_+} \frac{\gamma-1}{\gamma+1} + 1} \right) u_*^2 + p_* \\ \mathcal{H}_{\rho v}^{\delta I} = \rho_+ \left( \frac{\frac{p_*}{p_+} + \frac{\gamma-1}{\gamma+1}}{\frac{p_*}{p_+} \frac{\gamma-1}{\gamma+1} + 1} \right) u_* v_+ \\ \mathcal{H}_{\rho w}^{\delta I} = \rho_+ \left( \frac{\frac{p_*}{p_+} + \frac{\gamma-1}{\gamma+1}}{\frac{p_*}{p_+} \frac{\gamma-1}{\gamma+1} + 1} \right) u_* w_+ \\ \mathcal{H}_E^{\delta I} = u_* \left[ \frac{p_*}{\gamma-1} + \frac{1}{2} \rho_+ \left( \frac{\frac{p_*}{p_+} + \frac{\gamma-1}{\gamma+1}}{\frac{p_*}{p_+} \frac{\gamma-1}{\gamma+1} + 1} \right) (u_*^2 + v_+^2 + w_+^2) + p_* \right] \end{array} \right. \quad (62)$$

- Negative particle speed in the region between the two nonlinear waves,  $u_* < 0$

1. Right rarefaction -  $\mathbf{q}_-$ : if  $p_* \leq p_-$  and  $u_- + c_- \leq 0$  then we have a right rarefaction wave and the state in  $x/t = 0$  is the right state. The boundary fluxes are

$$\left\{ \begin{array}{l} \mathcal{H}_\rho^{\delta I} = \rho_- u_- \\ \mathcal{H}_{\rho u}^{\delta I} = \rho_- u_-^2 + p_- \\ \mathcal{H}_{\rho v}^{\delta I} = \rho_- u_- v_- \\ \mathcal{H}_{\rho w}^{\delta I} = \rho_- u_- w_- \\ \mathcal{H}_E^{\delta I} = u_- \left[ \frac{p_-}{\gamma-1} + \frac{1}{2} \rho_- (u_-^2 + v_-^2 + w_-^2) + p_- \right] \end{array} \right. \quad (63)$$

2. Right rarefaction -  $\mathbf{q}_{*-}$ : if  $p_* \leq p_-$ ,  $u_- + c_- > 0$  and  $u_* + c_- \left( \frac{p_*}{p_-} \right)^{\frac{\gamma-1}{2\gamma}} \geq 0$ , then we have a right rarefaction wave and the state for  $x/t = 0$  is the star right state. The boundary fluxes in this case are

$$\left\{ \begin{array}{l} \mathcal{H}_\rho^{\delta I} = \rho_- \left( \frac{p_*}{p_-} \right)^{\frac{1}{\gamma}} u_* \\ \mathcal{H}_{\rho u}^{\delta I} = \rho_- \left( \frac{p_*}{p_-} \right)^{\frac{1}{\gamma}} u_*^2 + p_* \\ \mathcal{H}_{\rho v}^{\delta I} = \rho_- \left( \frac{p_*}{p_-} \right)^{\frac{1}{\gamma}} u_* v_- \\ \mathcal{H}_{\rho w}^{\delta I} = \rho_- \left( \frac{p_*}{p_-} \right)^{\frac{1}{\gamma}} u_* w_- \\ \mathcal{H}_E^{\delta I} = u_* \left[ \frac{p_*}{\gamma-1} + \frac{1}{2} \rho_- \left( \frac{p_*}{p_-} \right)^{\frac{1}{\gamma}} (u_*^2 + v_-^2 + w_-^2) + p_* \right] \end{array} \right. \quad (64)$$

3. Right rarefaction -  $\mathbf{q}_{-Fan}$ : if  $p_* \leq p_-$ ,  $u_- + c_- > 0$  and  $u_* + c_- \left( \frac{p_*}{p_-} \right)^{\frac{\gamma-1}{2\gamma}} < 0$  we have a right rarefaction wave with a right state which is supersonic and the state for  $x/t = 0$  is the rarefaction fan. The boundary fluxes in this case are

$$\left\{ \begin{array}{l} \mathcal{H}_\rho^{\delta I} = \rho_- \left[ \frac{2}{\gamma+1} - \frac{\gamma-1}{\gamma+1} \left( \frac{u_-}{c_-} \right) \right]^{\frac{2}{\gamma-1}} \left( -\frac{2c_-}{\gamma+1} + \frac{\gamma-1}{\gamma+1} u_- \right) \\ \mathcal{H}_{\rho u}^{\delta I} = \rho_- \left[ \frac{2}{\gamma+1} - \frac{\gamma-1}{\gamma+1} \left( \frac{u_-}{c_-} \right) \right]^{\frac{2}{\gamma-1}} \left( -\frac{2c_-}{\gamma+1} + \frac{\gamma-1}{\gamma+1} u_- \right)^2 + p_- \left[ \frac{2}{\gamma+1} - \frac{\gamma-1}{\gamma+1} \left( \frac{u_-}{c_-} \right) \right]^{\frac{2\gamma}{\gamma-1}} \\ \mathcal{H}_{\rho v}^{\delta I} = \rho_- \left[ \frac{2}{\gamma+1} - \frac{\gamma-1}{\gamma+1} \left( \frac{u_-}{c_-} \right) \right]^{\frac{2}{\gamma-1}} \left( \frac{2c_-}{\gamma+1} - \frac{\gamma-1}{\gamma+1} u_- \right) v_- \\ \mathcal{H}_{\rho w}^{\delta I} = \rho_- \left[ \frac{2}{\gamma+1} - \frac{\gamma-1}{\gamma+1} \left( \frac{u_-}{c_-} \right) \right]^{\frac{2}{\gamma-1}} \left( \frac{2c_-}{\gamma+1} - \frac{\gamma-1}{\gamma+1} u_- \right) w_- \\ \mathcal{H}_E^{\delta I} = \left( -\frac{2c_-}{\gamma+1} + \frac{\gamma-1}{\gamma+1} u_- \right) \left\{ \frac{p_- \left[ \frac{2}{\gamma+1} - \frac{\gamma-1}{\gamma+1} \left( \frac{u_-}{c_-} \right) \right]^{\frac{2\gamma}{\gamma-1}}}{\gamma-1} + \right. \\ \left. + \frac{1}{2} \rho_- \left[ \frac{2}{\gamma+1} - \frac{\gamma-1}{\gamma+1} \left( \frac{u_-}{c_-} \right) \right]^{\frac{2}{\gamma-1}} \left[ \left( -\frac{2c_-}{\gamma+1} + \frac{\gamma-1}{\gamma+1} u_- \right)^2 + v_-^2 + w_-^2 \right] + \right. \\ \left. + p_- \left[ \frac{2}{\gamma+1} - \frac{\gamma-1}{\gamma+1} \left( \frac{u_-}{c_-} \right) \right]^{\frac{2\gamma}{\gamma-1}} \right\} \end{array} \right. \quad (65)$$

4. Right shock -  $\mathbf{q}_-$ : if  $p_* > p_-$  and  $u_- + c_- \left[ \frac{\gamma+1}{2\gamma} \left( \frac{p_*}{p_-} \right) + \frac{\gamma-1}{2\gamma} \right] \leq 0$  we have a right shock with

the state for  $x/t = 0$  being the right state. The associated boundary fluxes are

$$\begin{cases} \mathcal{H}_\rho^{\delta I} = \rho_- u_- \\ \mathcal{H}_{\rho u}^{\delta I} = \rho_- u_-^2 + p_- \\ \mathcal{H}_{\rho v}^{\delta I} = \rho_- u_- v_- \\ \mathcal{H}_{\rho w}^{\delta I} = \rho_- u_- w_- \\ \mathcal{H}_E^{\delta I} = u_- \left[ \frac{p_-}{\gamma-1} + \frac{1}{2} \rho_- (u_-^2 + v_-^2 + w_-^2) + p_- \right] \end{cases} \quad (66)$$

5. Right shock -  $\mathbf{q}_{*-}$ : if  $p_* > p_-$  and  $u_- + c_- \left[ \frac{\gamma+1}{2\gamma} \left( \frac{p_*}{p_-} \right) + \frac{\gamma-1}{2\gamma} \right] > 0$  we have a right shock with the state for  $x/t = 0$  being the star right state. The associated boundary fluxes are

$$\begin{cases} \mathcal{H}_\rho^{\delta I} = \rho_- \left( \frac{\frac{p_*}{p_-} + \frac{\gamma-1}{\gamma+1}}{\frac{p_*}{p_-} \frac{\gamma-1}{\gamma+1} + 1} \right) u_* \\ \mathcal{H}_{\rho u}^{\delta I} = \rho_- \left( \frac{\frac{p_*}{p_-} + \frac{\gamma-1}{\gamma+1}}{\frac{p_*}{p_-} \frac{\gamma-1}{\gamma+1} + 1} \right) u_*^2 + p_* \\ \mathcal{H}_{\rho v}^{\delta I} = \rho_- \left( \frac{\frac{p_*}{p_-} + \frac{\gamma-1}{\gamma+1}}{\frac{p_*}{p_-} \frac{\gamma-1}{\gamma+1} + 1} \right) u_* v_- \\ \mathcal{H}_{\rho w}^{\delta I} = \rho_- \left( \frac{\frac{p_*}{p_-} + \frac{\gamma-1}{\gamma+1}}{\frac{p_*}{p_-} \frac{\gamma-1}{\gamma+1} + 1} \right) u_* w_- \\ \mathcal{H}_E^{\delta I} = u_* \left[ \frac{p_*}{\gamma-1} + \frac{1}{2} \rho_- \left( \frac{\frac{p_*}{p_-} + \frac{\gamma-1}{\gamma+1}}{\frac{p_*}{p_-} \frac{\gamma-1}{\gamma+1} + 1} \right) (u_*^2 + v_-^2 + w_-^2) + p_* \right] \end{cases} \quad (67)$$

Note that the pressure in the star region,  $p_*$ , is pre-calculated from the following nonlinear equation

$$f(p_*, \mathbf{q}_+, \mathbf{q}_-) = f_+(p_*, \mathbf{q}_+) + f_-(p_*, \mathbf{q}_-) + u_- - u_+ = 0 \quad (68)$$

where

$$\begin{cases} f_+(p_*, \mathbf{q}_+) = (p_* - p_+) \left[ \frac{\frac{2}{(\gamma+1)p_+}}{p_* + \frac{(\gamma-1)}{(\gamma+1)} p_+} \right] & \text{if } p_* > p_+ \text{ (shock)} \\ f_+(p_*, \mathbf{q}_+) = \frac{2c_+}{(\gamma-1)} \left[ \left( \frac{p_*}{p_+} \right)^{\frac{\gamma-1}{2\gamma}} - 1 \right] & \text{if } p_* \leq p_+ \text{ (rarefaction)} \\ f_-(p_*, \mathbf{q}_-) = (p_* - p_-) \left[ \frac{\frac{2}{(\gamma+1)p_-}}{p_* + \frac{(\gamma-1)}{(\gamma+1)} p_-} \right] & \text{if } p_* > p_- \text{ (shock)} \\ f_-(p_*, \mathbf{q}_-) = \frac{2c_-}{(\gamma-1)} \left[ \left( \frac{p_*}{p_-} \right)^{\frac{\gamma-1}{2\gamma}} - 1 \right] & \text{if } p_* \leq p_- \text{ (rarefaction).} \end{cases} \quad (69)$$

After having pre-calculated the pressure  $p_*$ , the velocity in the star region,  $u_*$ , is calculated as follows:

$$u_* = \frac{1}{2}(u_+ + u_-) + \frac{1}{2}[f_-(p_*) + f_+(p_*)] \quad (70)$$

**HLL :**

The HLL (Harten, Lax, van Leer) Riemann solver is an approximated solver which assumes a two-wave configuration by neglecting the middle contact wave (i.e. neglecting the shear waves). The possible patterns in this case are three and they are selected through the evaluation of the fastest signal velocities which perturb the initial data, namely,  $S_+$  and  $S_-$

$$\begin{cases} S_L = \min(u_+ - c_+, u_{Roe} - c_{Roe}) \\ S_R = \max(u_- + c_-, u_{Roe} + c_{Roe}), \end{cases} \quad (71)$$

where  $u_{Roe}$  and  $c_{Roe}$  are the Roe averages of the normal speed and of the speed of sound respectively.

1.  $S_L \geq 0$

$$\begin{cases} \mathcal{H}_\rho^{\delta I} = \rho_+ u_+ \\ \mathcal{H}_{\rho u}^{\delta I} = \rho_+ u_+^2 + p_+ \\ \mathcal{H}_{\rho v}^{\delta I} = \rho_+ u_+ v_+ \\ \mathcal{H}_{\rho w}^{\delta I} = \rho_+ u_+ w_+ \\ \mathcal{H}_E^{\delta I} = u_+ \left[ \frac{p_+}{\gamma-1} + \frac{1}{2} \rho_+ (u_+^2 + v_+^2 + w_+^2) + p_+ \right] \end{cases} \quad (72)$$



2.  $S_- \leq 0$

$$\begin{cases} \mathcal{H}_\rho^{\delta I} = \rho_- u_- \\ \mathcal{H}_{\rho u}^{\delta I} = \rho_- u_-^2 + p_- \\ \mathcal{H}_{\rho v}^{\delta I} = \rho_- u_- v_- \\ \mathcal{H}_{\rho w}^{\delta I} = \rho_- u_- w_- \\ \mathcal{H}_E^{\delta I} = u_- \left[ \frac{p_-}{\gamma-1} + \frac{1}{2} \rho_R (u_-^2 + v_-^2 + w_-^2) + p_- \right] \end{cases} \quad (73)$$

3.  $S_+ < 0$  or  $S_- > 0$

$$\begin{cases} \mathcal{H}_\rho^{\delta I} = \frac{S_- \rho_+ u_+ - S_+ \rho_- u_- + S_- S_+ (\rho_- - \rho_+)}{S_- - S_+} \\ \mathcal{H}_{\rho u}^{\delta I} = \frac{S_- (\rho_+ u_+^2 + p_+) - S_+ (\rho_- u_-^2 + p_-) + S_- S_+ (\rho_- u_- - \rho_+ u_+)}{S_- - S_+} \\ \mathcal{H}_{\rho v}^{\delta I} = \frac{S_- (\rho_+ u_+ v_+) - S_+ (\rho_- u_- v_-) + S_- S_+ (\rho_- v_- - \rho_+ v_+)}{S_- - S_+} \\ \mathcal{H}_{\rho w}^{\delta I} = \frac{S_- (\rho_+ u_+ w_+) - S_+ (\rho_- u_- w_-) + S_- S_+ (\rho_- w_- - \rho_+ w_+)}{S_- - S_+} \\ \mathcal{H}_E^{\delta I} = \frac{S_- u_+ (E_+ + p_+) - S_+ u_- (E_- + p_-) + S_- S_+ (E_- - E_+)}{S_- - S_+} \end{cases} \quad (74)$$

It should be noted that the HLL Riemann solver does not allow for jumps in the tangential velocities as well as in the density. This feature can penalise some problems but can be beneficial for others such as the no-slip BCs.

#### HLLC :

The HLLC (Harten, Lax, van Leer + Contact) Riemann solver is an approximated solver which restores a three-wave configuration by contrast to the HLL solver. The possible patterns in this case are 4 and they are selected through the evaluation of the fastest signal velocities which perturb the initial data, namely,  $S_+$  and  $S_-$  (computed as in Eq. (71)) as well as through the calculation of the middle (contact) wave speed  $S_M$ :

$$S_M = \frac{p_- - p_+ + \rho_+ u_+ (S_+ - u_+) - \rho_- u_- (S_- - u_-)}{\rho_+ (S_+ - u_+) - \rho_- (S_- - u_-)} \quad (75)$$

1.  $S_L \geq 0$

$$\begin{cases} \mathcal{H}_\rho^{\delta I} = \rho_+ u_+ \\ \mathcal{H}_{\rho u}^{\delta I} = \rho_+ u_+^2 + p_+ \\ \mathcal{H}_{\rho v}^{\delta I} = \rho_+ u_+ v_+ \\ \mathcal{H}_{\rho w}^{\delta I} = \rho_+ u_+ w_+ \\ \mathcal{H}_E^{\delta I} = u_+ \left[ \frac{p_+}{\gamma-1} + \frac{1}{2} \rho_L (u_+^2 + v_+^2 + w_+^2) + p_+ \right] \end{cases} \quad (76)$$

2.  $S_- \leq 0$

$$\begin{cases} \mathcal{H}_\rho^{\delta I} = \rho_- u_- \\ \mathcal{H}_{\rho u}^{\delta I} = \rho_- u_-^2 + p_- \\ \mathcal{H}_{\rho v}^{\delta I} = \rho_- u_- v_- \\ \mathcal{H}_{\rho w}^{\delta I} = \rho_- u_- w_- \\ \mathcal{H}_E^{\delta I} = u_- \left[ \frac{p_-}{\gamma-1} + \frac{1}{2} \rho_R (u_-^2 + v_-^2 + w_-^2) + p_- \right] \end{cases} \quad (77)$$

3.  $S_+ < 0$  and  $S_M \geq 0$

$$\begin{cases} \mathcal{H}_\rho^{\delta I} = \rho_+ u_+ + S_+ \left[ \rho_+ \frac{(S_+ - u_+)}{(S_+ - S_M)} - \rho_+ \right] \\ \mathcal{H}_{\rho u}^{\delta I} = \rho_+ u_+^2 + p_+ + S_+ \left[ \rho_+ \frac{(S_+ - u_+)}{(S_+ - S_M)} - \rho_+ u_+ \right] \\ \mathcal{H}_{\rho v}^{\delta I} = \rho_+ u_+ v_+ + S_+ \left[ \rho_+ \frac{(S_+ - v_+)}{(S_+ - S_M)} - \rho_+ v_+ \right] \\ \mathcal{H}_{\rho w}^{\delta I} = \rho_+ u_+ w_+ + S_+ \left[ \rho_+ \frac{(S_+ - w_+)}{(S_+ - S_M)} - \rho_+ w_+ \right] \\ \mathcal{H}_E^{\delta I} = u_+ (E_+ + p_+) + S_+ \left\{ \rho_+ \frac{(S_+ - u_+)}{(S_+ - S_M)} \left[ \frac{E_+}{\rho_+} + (S_M - u_+) \left( S_M + \frac{p_+}{\rho_+ (S_+ - u_+)} \right) \right] - E_+ \right\} \end{cases} \quad (78)$$

4.  $S_M < 0$  and  $S_- > 0$

$$\left\{ \begin{array}{l} \mathcal{H}_\rho^{\delta I} = \rho_- u_- + S_- \left[ \rho_- \frac{(S_- - u_-)}{(S_- - S_M)} - \rho_- \right] \\ \mathcal{H}_{\rho u}^{\delta I} = \rho_- u_-^2 + p_- + S_- \left[ \rho_- \frac{(S_- - u_-)}{(S_- - S_M)} - \rho_- u_- \right] \\ \mathcal{H}_{\rho v}^{\delta I} = \rho_- u_- v_- + S_- \left[ \rho_- \frac{(S_- - v_-)}{(S_- - S_M)} - \rho_- v_- \right] \\ \mathcal{H}_{\rho w}^{\delta I} = \rho_- u_- w_- + S_- \left[ \rho_- \frac{(S_- - w_-)}{(S_- - S_M)} - \rho_- w_- \right] \\ \mathcal{H}_E^{\delta I} = u_- (E_- + p_-) + S_- \left\{ \rho_- \frac{(S_- - u_-)}{(S_- - S_M)} \left[ \frac{E_-}{\rho_-} + (S_M - u_-) \left( S_M + \frac{p_-}{\rho_- (S_- - u_-)} \right) \right] - E_- \right\} \end{array} \right. \quad (79)$$

For a more detailed discussion and some additional implementative insights on this topic the interested reader can refer to Toro.<sup>20</sup>

## References

- <sup>1</sup>Abbas, Q., and Nordström, J., *Weak Versus Strong No-Slip Boundary Conditions for the Navier-Stokes Equations*, Engineering Applications of Computational Fluid Mechanics, 2010.
- <sup>2</sup>Albin, E., D'Angelo, Y. and Vervisch, L. *Flow streamline based Navier-Stokes Characteristic Boundary Conditions: Modeling for transverse and corner outflows*, Computers & Fluids, 2011
- <sup>3</sup>Bassi, F. and Rebay, S. *A High-Order Accurate Discontinuous Finite Element Method for the Numerical Solution of the Compressible Navier-Stokes Equations*, Journal of Computational Physics, 1997
- <sup>4</sup>Cockburn B., Shu C.-W., *The Local Discontinuous Galerkin Method for Time-Dependent Convection-Diffusion Systems* SIAM J. Numer. Anal., Volume 35, Issue 6, 1998
- <sup>5</sup>Peraire J., Persson P.-O. *The Compact Discontinuous Galerkin (CDG) Method for Elliptic Problems* SIAM J. Sci. Comput., Volume 30, Issue 4, 2008
- <sup>6</sup>Arnold D. N., *An interior penalty finite element method with discontinuous element* SIAM J Numer Anal Volume 19, Issue 4, 1982
- <sup>7</sup>Eliasson, P., Eriksson, S. and Nordström, J., *Influence of Weak and Strong Solid Wall Boundary Conditions on the Convergence to Steady-State of the Navier-Stokes Equations*, AIAA Computational Fluid Dynamics, 2009
- <sup>8</sup>Nordström, J., Eriksson, S. and Eliasson, P., *Weak and strong wall boundary procedures and convergence to steady-state of the Navier-Stokes equations* Journal of Computational Physics, 2012
- <sup>9</sup>Liu, H. and Xu, K., *A Runge-Kutta discontinuous Galerkin Method for Viscous Flow Equations*, Journal of Computational Physics, 2007
- <sup>10</sup>Lodato, Guido and Domingo, Pascale and Vervisch, Luc, *Three-Dimensional Boundary Conditions for Direct and Large-Eddy Simulation of Compressible Viscous Flows*, Journal of Computational Physics, 2008
- <sup>11</sup>Poinsot, T.J. and Lele, S.K., *Boundary conditions for Direct Simulations of Compressible Viscous Flows*, Journal of Computational Physics, 1992
- <sup>12</sup>Thompson, W., *Time Dependent Boundary Conditions for Hyperbolic Systems*, Journal of Computational Physics, 1987, Volume 68, Issue 1
- <sup>13</sup>Thompson, W., *Time-Dependent Boundary Conditions for Hyperbolic Systems, II*, Journal of Computational Physics, 1990, Volume 89, Issue 2
- <sup>14</sup>Giles M.B. *Nonreflecting Boundary Conditions for Euler Equation Calculations*, AIAA Journal, 1990, Volume 28, No. 12
- <sup>15</sup>Huynh H.T., *A Flux Reconstruction approach to high-order schemes including discontinuous Galerkin methods*, AIAA Computational Fluid Dynamics, 2007
- <sup>16</sup>Vincent P.E. Castonguay P. Jameson A., *A new class of high-order energy stable Flux Reconstruction schemes*, Journal of Sci Comput, 2011
- <sup>17</sup>Castonguay P. Vincent P.E. Jameson A., *A new class of high-order energy stable Flux Reconstruction schemes for triangular elements*, Journal of Sci Comput, 2011
- <sup>18</sup>Hesthaven J.S., Warburton T., *Nodal Discontinuous Galerkin Methods* Springer, 2007
- <sup>19</sup>Karniadakis G.E., Sherwin S., *Spectral/hp Element Methods for Computational Fluid Dynamics* Oxford Science Publications, 2005
- <sup>20</sup>Toro E.F., *Riemann Solvers and Numerical Methods for Fluid Dynamics* Springer, 2009
- <sup>21</sup>Colonius T., *Modelling Artificial Boundary Conditions for Compressible Flow* Annu. Rev. Fluid Mech, 2004
- <sup>22</sup>Polifke W., Wall C., Moin P., *Partially reflecting and non-reflecting boundary conditions for simulation of compressible viscous flow* Journal of Computational Physics, 2006
- <sup>23</sup>Mani A., *Analysis and optimization of numerical sponge layers as a nonreflective boundary treatment* Journal of Computational Physics, 2012
- <sup>24</sup>Pirozzoli S., Colonius T., *Generalized characteristic relaxation boundary conditions for unsteady compressible flow simulations* Journal of Computational Physics, 2013